Cylindrical Cross-Bars for Thermal Performance Augmentation in Air Channel

Frans J. J. Coetzee[*]

Email: u11119595@tuks.co.za

Gazi I. Mahmood[*,1]

Email: gmahmood@pmu.edu.sa

[*]University of Pretoria, Hatfield, Pretoria, South Africa.

[1]Department of Mechanical Engineering, Prince Mohammad Bin Fahd University, Al-Khobar, Saudi Arabia.

Abstract

Experiments of the heat transfer and pressure drop are performed in a rectangular channel employing eight different arrays of cylindrical cross-bars as inserts. Numerical simulations are also performed to examine the secondary flow caused by the cylinders. The objectives are to investigate the enhancement of the channel-wall heat transfer and pressure drop caused by the local flow, cylinder array geometry, and flow Reynolds number. Two different cylinder diameters of 1.0 mm and 2.0 mm are employed. The diameter of 2.0 mm is used to create four in-line arrays while the diameter of 1.0 mm is used to create four staggered arrays of the cylinders. The cylinder arrays employ different diameter-to-pitch ratios (0.025 to 0.2) and cylinder orientations (45°, 90°) relative to the main flow direction. The flow Reynolds number is varied between 600 and 13000. Only two array geometries, one in-line and one staggered, with the cylinders oriented at 90° to the flow are modelled for the numerical study. The numerical results show the local flow accelerates in the gap between the cylinder and channel

[1] Corresponding author, Phone: +966138498514.

wall. The vortex shedding downstream of the cylinders interacts with the channel wall. The Nusselt number on the channel wall and friction factor are measured with and without the cylinders. The ratios of Nusselt numbers and friction factors increase with the Reynolds number when the Reynolds number is less than 3000. The ratios always increase with the diameter-to-pitch ratio.

Keywords: *Heat transfer enhancement; Pressure drop enhancement; Vortex shedding; Nusselt number; Friction factor; Thermal performance.*

1. Introduction

The internal convection of heat transfer in the channel flow applications is enhanced commonly by employing the different forms of roughened walls, turbulators, inserts, and porous metal foams. A major drawback of employing these structures is that the accompanying pressure penalty in the flow also increases. Consequently, the thermal performance of the channel providing the heat transfer to or from the fluid for a given flow pumping power is not improved appreciably compared to that of the smooth channel. Also, the heat exchangers and heating or cooling channels of fluids in many applications requiring small pumping power cannot employ the heat transfer augmentation structures imposing the high pressure penalty. The flow blockage and secondary turbulent flows or profile drag caused by the augmentation structures are responsible for the high-pressure penalty. The present study employs the arrays of cylindrical cross-bars in a rectangular air channel to experimentally and computationally investigate the flow field, pressure drop, and convection heat transfer in the channel. The thermal performances of the channel with and without the cylindrical cross-bars are compared with each other for the applicability, effectiveness, and competitiveness of the cylindrical bars as the heat transfer augmentation device. The advantages of the cylindrical cross-bars are as

follows: (i) the profile drag on the cylinders in the cross-flow is smaller than many heat transfer augmentation devices, (ii) the wake flow downstream of the cylinder can enhance the near-wall turbulent mixing and heat transfer, and (iii) the construction and deployment of the cylinder arrays are simple and cheap.

The experimental study of the circular-tube flow by Eiamsa-Ard et al. (2015) compared the thermal performance of dual-and-triple twisted helical tapes with that of single twisted helical tapes. The measured thermal performance coefficient in the study decreased as the Reynolds number increased for all the tested configurations. The thermal performance coefficients of the double and triple-helical twisted tapes were better than those of the single-helical twisted tape. Helical coil tapes were inserted in a rectangular duct by Kumar and Layek (2018) to measure the effects of coil geometry on heat transfer and pressure drop at high Reynolds numbers. The measurements found an optimal coil pitch for the high heat transfer coefficients without having a large effect on the pressure penalty. The numerical models of rib-roughened walls of Li et al. (2000), Sahu et al. (2019), and Zheng et al. (2019) produced the thermal performance coefficients of values less than 1.0 in rectangular channel flows when the Reynolds numbers were high because of the large pressure drops irrespective of the rib geometries. The pin-fins are commonly employed in the rectangular channel flow to augment heat transfer at the walls. Eren and Caliskan (2016) experimented with the cylindrical and triangular grooved pin-fins. The triangular grooved pin-fins outperformed the cylindrical grooved pin-fins for the thermal performance coefficient for the entire range of Reynolds number tested.

A very limited number of investigations on the aerothermal behaviour of channel flows with the eddy promoting bars as inserts is reported in the literature. Leonardi et al. (2015) compared the computed thermal performance of wall mounted circular and square bars in a channel flow. The study found that the maximum heat transfer difference between the two shapes was less than 5%, but that the pressure penalty for the circular bars was 12% less than that for the square

bars. Vujisic (1994) tested the cylindrical cross-bars as the turbulence or eddy promoters in the rectangular channel flow. Compared to the plane channel data at the high Reynolds numbers, the measured heat transfer augmentation at the wall due to the cylindrical bars gradually diminished. The experimental results of Mikic et al. (1992) found the cylindrical eddy promoters reduced the Reynolds number for transition to the turbulent flow in a rectangular channel. However, the transition Reynolds number based on the wall friction velocity with and without the cylindrical turbulators were about the same.

The primary focus of the previous investigations in the channel flow employing the intrusive type wall structures and inserts such ribs, pin-fins, helical inserts, and cross-bars was to enhance the heat transfer at the wall. Limiting the pressure or pumping power rise along with the heat transfer enhancement was not the primary goal in those investigations. The investigations were also limited in the turbulent flow regime of the incoming flow. In the present investigation, the cylindrical bars in the channel are employed in arrays in the 90° and 45° cross-flow arrangements relative to the main flow. The adiabatic cylinders are placed either one-diameter or 0.75-diameter away from the heater transfer walls of the channel and employed as inserts for easy replacements. The objectives of the investigation are to increase the thermal performance of the channel by: (i) enhancing the convection heat transfer at the channel walls primarily by the flow accelerations and turbulent wakes generated by the cylinders, and (ii) limiting the increase in the pressure penalty as the drag coefficient of the cylinders in the cross-flow is smaller than many flow turbulators. Eight arrays of the cylinders of the same geometry are tested. Measurements of the pressure drop and wall heat transfer along the channel are presented at the Reynolds numbers ranging from the laminar to the turbulent flow regimes. The local flow structures are also investigated by the computational models of few test cases to provide some detail physics of the local heat transfer enhancements.

2. Experimental set-up

2.1. Wind tunnel

Figure 1 shows a schematic diagram of the low-speed wind tunnel housing the test section. The open-loop tunnel operates under the suction of a centrifugal blower. The main components of the tunnel consist of a two-dimensional contraction section, a flow developing section, a test section, and an exit section. The flow cross-section of the sections is rectangular. The tunnel-walls are made of high density woods of thickness 12 mm. The two-dimensional contraction of reduction ratio 27:1 with honeycomb screens at the inlet accelerates the ambient air smoothly and delivers the flow into the flow developing section. The flow develops in the 2.0 m long section before entering the test section. The test section is 0.50 m long where the cylindrical cross-bar array is placed as an insert. The flow from the test section enters into the 0.50 m long exit section and then into a large wooden plenum box as shown in Fig. 1. Two pipes of diameter 101 mm and 50 mm equipped with valves deliver the air flow from the exit plenum to another large plenum connected to the blower suction-inlet. The pipes are metered with the ISO-standard (International Organization for Standardization) orifice plate-flange assemblies. The blower speed is controlled by a variable speed drive. The mass flow rate in the tunnel is controlled by the combination of the blower speed and valve openings. For the laminar flow, only the pipe of diameter 50 mm is operated.

The height of the rectangular cross-section of the wind-tunnel section can be adjusted to vary the cross-section. The width of the cross-section is fixed to 203 mm. Most of the tests are conducted at the constant tunnel height of H = 5 mm and aspect ratio (W/H) of 0.025:1. Few of the tests are conducted at a height of H = 25 mm to validate the computational models of some cylindrical-bar arrays.

2.2. Cylindrical cross-bar configurations

Figure 2 shows an actual image of an array of cylinders and the placement of the cylindrical bars in the test section. The cylinders are made of the commercial stainless steel rods. Thin spacer-strips are employed to hold the cylinders in the desired position inside the array. The cylinders in the arrays are arranged in the cross-flow orientation either with the θ = 90° or θ = 45° to the main flow in the test section. The pitch (p) between the cylinders, diameter (d) of cylinders, and angle (θ) to the direction of the flow are varied to form eight different arrays of cylinders. The arrays extend from the inlet to exit of the test section. Table 1 provides the descriptions of the cylinder arrays. The 1-mm or 5-mm diameter cylinders are employed in the staggered array, and the 2-mm or 10-mm diameter cylinders are employed in the in-line array. The frontal blockage ratio of cylinder frontal area to channel cross-sectional area is 0.40 ($2d/H$ for d =1 mm and d/H for d = 2 mm) for all the array arrangements. Test results for the cases of (d = 5 mm, p = 100 mm, θ = 90°) and (d = 10 mm, p = 50 mm, θ = 90°) in Table 1 are used to validate the computational models of the same array cases. The channel height (H) is 25 mm for the validation cases. The geometry of the validation cases is made 5 times the geometry of the cases at the channel height, H = 5 mm to obtain the wall pressure data with the high spatial resolutions.

The cylindrical rods are supported by six evenly spaced bar-strips of thickness 1 mm which are made of a plastic. The strip-height of 5 mm or 25 mm makes strips also act as spacers between the two channel-walls separated by the height, H. Figure 2(a) shows that the support bar-strips are placed parallel to the mean flow. The assembly of bar-strips and cylindrical rods fits snugly in the test section. Because the strips isolate the cylinders from the heated walls of the channel, the cylinder surfaces are considered adiabatic. The spacer bars can be employed as the structural supports for the plate heat-exchanger walls when the cylinder arrays are inserted as the flow turbulators. The measurements of two cases of θ = 45° and 90° for (d = 1

mm, p = 20 mm) in Table 1 and two cases of θ = 45° and 90° for (d = 2 mm, p = 20 mm) with the same pitch-spacing are obtained to show the effects of the cylinder diameter and cylinder array orientation angle (θ). The remaining cases in Table 1 are tested to show the effects of the pitch-spacing and θ at a given cylinder diameter.

2.3. Instrumentations

One of the two 203 mm wide walls of the test section is fitted with drilled pressure taps of diameter 0.3 mm. The taps are distributed along the main flow direction at 15 mm apart from each other for the H = 5 mm channel or 1.0 mm apart for the H = 25 mm channel. All the taps are located along the mid-width positions ($W/2$) of the wall. In the channel with H = 25 mm, the 17th cylinder from the inlet of test section is a tube and has a wall-pressure tap of diameter 0.3 mm located away from the cylinder ends. This cylinder can be rotated about the axis to read the pressure signals at different angular positions on the cylinder wall. All the pressure taps are connected to an electro-mechanical scanner via the plastic tubings. The scanner is connected to a differential pressure transducer via another port. The scanner port connects one pressure tap at a time to the pressure transducer when an electrical signal is triggered from a controller.

The 203 mm wide top and bottom walls of the test section are removable and can be replaced with the 6.0 mm thick Perspex plates. Commercially available silicone-rubber encapsulated electric resistance heaters are attached on the flow side of the Perspex plates as shown in Fig. 3 and cover the entire surface of both plates. The thickness of the heaters is 1.0 mm. The open side of the heaters to the air flow is placed flush with the upstream and downstream surfaces of the test section. The heaters are connected to a 600 watt DC power supply in the parallel connection and provide the same constant power flux along the walls. The current and voltage of the DC power supply can be adjusted to control the heat flux level. As shown in Fig. 3, the test section walls are insulated with two layers of polystyrene-foam (thermal conductivity = 0.041 W/m.K) during the heat transfer measurements. Thermocouples are placed between the insulation layers and between the insulation layer and

Perspex wall to measure the conduction heat loss to the ambient through the thicknesses. The heat transfer measurements are obtained in the H = 5 mm channel only.

Figure 3(b) also shows the locations of the thermocouple tips along the heated wall (bottom plate) in the test section. The thermocouples are embedded all along the bottom wall either with a 5 mm or a 10 mm spacing from each other. The distributions are located in the mid-width positions ($W/2$) of the wall. The thermocouple tips are inserted through drilled holes in the bottom plate and placed just adjacent to the heater. The holes are filled in with a thermally conductive paste. The thermocouples are of the T-type with the 32-gage wire diameter and calibrated in a wet thermal bath.

3. Measurement methods

All measurements are obtained when the flow reaches the quasi steady-state defined by the pressure and temperature changes by less than 2.0 Pa and 0.1°C, respectively, over a period of 10 minutes. The air flow is incompressible due to the small changes in the mean velocities and pressure across the test section. The voltage signals from the pressure transducer and thermocouples are acquired with a National Instrument™ data acquisition system via a Labview™ computer program. The signals from each acquisition channel are logged at 500 Hz for 2 seconds for the temperature and at 200 Hz for 6 seconds for the pressure. The voltage signals are then time-averaged and converted into the units of degree Celsius and Pascal after applying the appropriate calibration curves.

The air-mass flow rate is measured with the orifice plates located in the pipe sections following the exit plenum in Fig. 1. The discharge coefficient for the orifice plate at each measured pressure drop across the orifice is determined from the Stolz equation in ISO 5167-1:1991 through iterations. The air properties for the mass flow measurements are determined from the ideal gas law at the measured air temperature downstream of the orifice plate. The flow Reynolds number in the channel is then obtained from the mass flow rate and test-channel hydraulic diameter.

Only the flow-side surfaces of the 203-mm wide top and bottom plates are heated for the heat transfer measurements in the test section. The thermal boundary layer thus starts as the ambient air enters the test section. As the surface heaters on the plates are in direct contact with the air-flow (refer to Fig. 3) and the test section walls are insulated, most of the heater power is convected into the air-flow. The conduction losses through the insulations are estimated based on the temperature differences across the insulation thickness and one-dimensional conduction analysis. The conduction losses normal to the wall found to be about 2.0% or less of the total heater power input. The maximum temperature difference between the heater surface and surrounding area is 35 °C to neglect the radiation losses from the heater. Mahmood et al. (2015) provides more details of the conduction loss estimations. The total power input to a heater is determined from the DC current and voltage drop across the heater. The convective power, Q_c into the flow from a heater is then the total heater power minus the conduction losses. The local mixed-mean temperature of air, $T_{m,x}$ along the test section in Eq. (1) is obtained from the energy balance in the test section from $x = 0$ to x. The local Nusselt number, Nu_x at a wall thermocouple position is then determined from the average convective heat flux, $Q_c/(L.W)$ in Eq. (2). The local convective flux is assumed to differ little from the average flux as the conduction losses are small. The current and voltage controls of the DC power supply ensure the same Q_c from the two heaters in the test section. The total power, $\sum Q_{c,x}$ in Eq. (1) is the total convective power from the two heaters over the length Δx. The thermal properties of the air (k_a, $C_{p,a}$) are determined at the inlet temperature of air, $T_{a,x=0}$ to the test section as the air temperature does not rise more than 25 ^{o}C across the test section. The inlet temperature is the same as the ambient temperature with no pre-heating upstream of the test section. The heater power input is controlled to maintain the difference of ($T_{w,x} - T_{m,x}$) to be between 10 °C and 15 °C to reduce the uncertainties in Nu_x in Eq. (2). The heater surface temperature, $T_{w,x}$ is obtained at a wall-thermocouple location. The thermocouple provided temperature on the wall-side of

the heater (refer to Fig. 3(b)) is assumed to be about the same as the local surface temperature, $T_{w,x}$ on the flow-side. This approximation introduces negligible errors in the estimated quantity which are confirmed later (refer to Fig. 17) by the good comparisons of the Nusselt numbers between the smooth channel case without the cylinder array and analytical cases.

$$T_{m,x} = \left(T_{a,x=0}\right) + \frac{\sum Q_{c,x}}{(\dot{m}\, C_{p,a})} \tag{1}$$

$$Nu_x = \frac{(Q_c\, D_h)}{(L.W.(T_{w,x} - T_{m,x}).k_a)} \tag{2}$$

4. Experimental uncertainties

The accuracy of the thermocouple is 0.1 °C and the pressure transducer is 2 Pa. The bias errors in the measurements are accounted for in the calibrations. The uncertainties in the calibrations, measurements, and calculated data are estimated based on Beckwith et al. (2007) and Moffat (1988). The details of uncertainty analyses are provided in Cramer (2018). The uncertainties in the pressure are 2.5 Pa at the minimum and 13.0 Pa at the maximum. The mass flow rate of air has the maximum uncertainty of ±5%. The uncertainties in the calculated *f* are then 2% at the minimum and 15% at the maximum. The maximum uncertainty in the temperature is 1.0 °C, heat flux is 4%, Nusselt number is 15%, and thermal performance coefficient is 20% when the *Re* < 1000. The uncertainties in the Nusselt number and thermal performance coefficients decrease when *R*e > 1000. The required fan speed at a low mass flow rate of air in the channel was difficult to maintain at a constant level with the commercial variable frequency drive. The variations in the fan speed at a low mass flow rate of air introduce high uncertainties in the measurements of pressure. The flow rate variations at low *Re* primarily contribute to the high uncertainties in the calculated data.

5. Computational model

Detailed measurements of the secondary flow-field are difficult in the H = 5 mm channel due to geometric constraints. Computational-fluid-dynamics (CFD) simulations are performed to show and explain the secondary flow-field in the wake of the cylindrical cross-bars. The secondary flows near the heated walls are responsible for the turbulent mixing and heat transfer augmentation. Many researchers in the past preferred the *k-Ω SST* turbulence model for good predictions of the near-wall separated flows. For example, the *k-Ω SST* models of Menter (1994), Fiebieg et al. (1994), Apsley and Leschziner (2000), Lotfi et al. (2016), and Sinha et al. (2016) predicted the experimental results of heat transfer and separated shear layer in the channel flows with good accuracy. The transient mode of the *k-Ω SST* model of the commercial CFD solver Ansys Fluent version 17.1 is, therefore, employed to simulate the flow-field in the cylinder arrays.

The experimental cases in the H = 25 mm channel of Table 1 tagged with the "*" sign are simulated: d/p = 0.05, θ = 90° where d = 5 mm and d/p = 0.2, θ = 90° where d = 10 mm. The two-dimensional domains for the experimental cases are modelled. The large aspect ratio of the channel (W/H = 8) causes negligible effects of the side-walls on the flow and renders the test channel to be virtually a parallel channel. Only eight cylinders are used in the simulations because the flow develops fully after only four cylinders in the streamwise direction as found from comparing the computational velocity profiles downstream of the cylinders. Figure 4(a, b) shows the computational domain in the channel. The domain flow-inlet is located 3.6H upstream and flow-exit is located 1.8H downstream of the 1st and last cylinder, respectively, for both in-line and staggered cylinder arrays. The boundary walls are also clearly identified in Fig. 4(a, b). The fully-developed velocity profile of a plane-parallel channel is employed at the inlet (x = 0). The pressure-outlet boundary condition is set at zero-gage pressure at the exit (x

= 52*H*). The boundary walls of channel and cylinders are set as the no-slip and adiabatic wall conditions. The working fluid is air with properties at the laboratory ambient conditions.

The computational domain is discretized with the quadrilateral cells. The cell geometry for both the in-line and staggered cylinder arrays are shown in Fig. 4(c). The maximum $y+$ value next to the boundary walls is 0.2. The cell inflation value is 0.1 on the cylinder boundaries and is 0.2 on the channel walls. The number of cells in the inflation layers is then 25 on the cylinder boundaries and 15 for the channel walls. The following solution steps in the Ansys-Fluent 17.1 are used: pressure-velocity coupling scheme, second-order pressure scheme, second-order upwind momentum scheme, first-order upwind turbulent kinetic energy solver, second-order implicit transient formulation. The convergence criterion is set to a residual of 10^{-6} for: continuity, *x*-velocity, *y*-velocity, *k*, and Ω equations.

Figure 5 and Figure 6 are used to test the dependence of numerical results on the cell size and number for the staggered and in-line cylinder array, respectively. The dependence is shown for the laminar *Re* = 920 and turbulent *Re* = 9700 as the number of cells is varied. The local streamwise (+*x* direction) velocity, $U_{H/4}$ in Fig. 5 and $U_{H/2}$ in Fig. 6 are the time-averaged results at 2.5*d* downstream of the streamwise 5th cylinder. The velocity ratios in the figures are obtained using the mass-averaged velocity, V_{avg} at *Re* = 920 and 9700. The ratios, $U_{H/4}/V_{avg}$ and $U_{H/2}/V_{avg}$ change less than by 1% when the number of cells is increased from 230E+03 to 360E+03 for the staggered array and from 210E+03 to 320E+03 for the in-line array. The subsequent numerical results presented in the paper are obtained with the latter number of cells for each array of cylinders.

The computational models of staggered and in-line cylinder array are validated by comparing the time-averaged results between the models and experiments in Figs. 7-10. The results are obtained for Re = 9700. Equation (3) defines the pressure coefficients, ΔP_α around the cylinder surface in Figs. 7 and 8 where $\alpha = 0°$ is located on the front stagnation point of the

cylinder. The ΔP_α distributions are obtained on the streamwise 6th cylinder for the models and 17th cylinder for the experiments. The value of ΔP_α in Figs. 7 and 8 increases away from the stagnation location of α = 0° due to the flow acceleration and pressure decrease along the cylinder surface. The pressure increases at about α > (±70°) as the flow decelerates causing the plateaus in ΔP_α distributions at α > (±70°). The numerical and experimental ΔP_α distributions in both Fig. 7 and Fig. 8 compare reasonably well with each other. The uncertainties in the correct α positions in the experiments contribute to the differences between the numerical and experimental data.

$$\Delta P_\alpha = \frac{P_{\alpha=0} - P_\alpha}{\frac{1}{2}\rho V_{avg}^2} \tag{3}$$

The pressure coefficients, ΔP_x of Figs. 9 and 10 are defined by Eq. (4) where the x = 0 refers to the wall-location corresponding to the cylinder stagnation position. The distributions of ΔP_x are shown along the channel wall corresponding to the streamwise 6th cylinder and it's downstream locations for the models and the streamwise 17th cylinder and it's downstream locations for the experiments. The sharp rise of ΔP_x distributions between -0.2 < (x/d) < 0.4 in Figs. 9 and 10 is caused by the flow acceleration in the decreasing space between the cylinder and wall. The subsequent fall of ΔP_x distributions between 0.4 < (x/d) < 1.0 is then caused by the flow deceleration in the increasing space between the cylinder and wall. The wall pressure, P_x then decreases and ΔP_x increases at (x/d) > 1.0 between the cylinders due to the pressure losses along the channel. The numerical ΔP_x distributions are fairly similar to the experimental ΔP_x distributions both in Fig. 9 and 10. The uncertainties in the correct x positions in the experiments contribute to the differences between the numerical and experimental data.

$$\Delta P_x = \frac{P_{x=0} - P_x}{\frac{1}{2}\rho V_{avg}^2} \tag{4}$$

6. Discussions of results

6.1. Velocity and vorticity fields (computations)

The numerical results of non-dimensional streamwise velocity (v_x^*) and *z*-vorticity (ω_z^*) are presented in Figs. 11 to 14 for *Re* = 920 and 9700 for the staggered and in-line cylinder arrays. The time dependence of the quantities is presented by plotting them at different non-dimensional times, *t** at a Reynolds number. Equations (5-7) are used to compute the quantities from the time dependent v_x, ω_x, and *t*. The time step, $\Delta t^* = 0.16$ between the consecutive plots and the total time lapse of 0.80 for the evolution of (ω_z^*, v_x^*) for a cylinder array are the same in all figures. The data in Figs. 11 to 14 are shown in the region between 1*H* upstream and 1*H* downstream of the streamwise 7th cylinder for both the staggered and in-line cylinder array. The time-average flow is fully developed when it reaches the downstream location of the 4th cylinder as indicated in Section 5. The origin of *y/H* = 0 is located at the mid-height (*H/2*) of the channel. The flow field is then shown along the entire channel height in the figures. The G in Fig. 11 represents the gap between the cylinder and channel wall. Note the ratio of G/d is 1.0 for the staggered and 0.75 for the in-line cylinders. However, the G/d ratio is 3.0 for the staggered cylinders when the 2nd wall of the channel at *y/H* = 0.5 is considered.

$$\omega_z^* = \frac{\omega_z H}{V_{avg}} \tag{5}$$

$$t^* = \frac{t\, V_{avg}}{H} \tag{6}$$

$$v_x{}^* = \frac{v_x}{V_{avg}} \tag{7}$$

The normalized (ω_z^*, v_x^*) distributions about the cylinder show the instantaneous interactions of the secondary flows downstream of the cylinder with the wall boundary layer as the *t** progresses. The unsteadiness and turbulence of the secondary flows break the wall boundary layer and promote the near wall flow-mixing, both of which cause the enhancement

of local heat transfer at the wall. Figure 11 and Figure 13 show the ω_z^* contours along with streamlines plotted using the velocity magnitudes. The high values of ω_z^* surrounding and downstream of the cylinder as well as the convoluted streamlines downstream of the cylinder indicate the evolution of vortex shedding with the t^*. The sizes of the vortex shedding regions can be scaled by the cylinder diameter. The high ω_z^* values adjacent to the channel walls at $y/H = \pm 0.5$ are caused by the near wall turbulence. Note the total time lapse from $t^* = 0.0$ to 0.80 may not represent the time-period of vortex shedding in Figs. 11 and 13. The vortex structures shedding from the cylinder and from the wall turbulent flow are closer to each other for the staggered cylinder in Figs. 11(a) and 13(a) than for the in-line cylinder in Figs. 11(b) and 13(b). The interactions of the vortices cause the near-wall flow to be lifted away from the wall at the downstream locations of the cylinder. The heat transfer is high at the wall downstream of the cylinders which is examined experimentally. Note that the streamlines and ω_z^* contours downstream of the cylinder interact with those from the two walls for the in-line cases (Figs. 11(b) and 13(b)). The consequence is the higher pressure drop along the flow for the in-line cylinders than for the staggered cylinders which is also examined experimentally. The convoluted streamlines in the channel with the cylinder arrays are responsible for the higher pressure drop than the smooth channel. The results of Salehi et al. (2018) and Jamalabadi and Oveisi (2016) showed the streamlines between the cylinder and bounding wall becamce more parallel to the wall as the *Re* increases.

The v_x^* contour distributions in Figs. 12 and 14 indicate the local flow accelerations between the cylinder and channel wall. The local accelerated flows cause the high mass flux and local heat transfer enhancement at the wall. The region of higher v_x^* values in the gap between cylinder and wall is always larger for the in-line cylinders than for the staggered cylinders at both $Re = 920$ and 9700. The flow accelerates when convecting from the low to high value v_x^* region. The local heat transfer rate at the wall in the cylinder location and downstream of the

cylinder is then expected to be higher. The v_x^* values are higher outside the vortex shedding regions. The sizes of the higher-valued v_x^* regions change little from Fig. 12 to Fig. 14 as the *R*e increases for both staggered and in-line cylinder arrays. The combination of flow-accelerations and secondary-flow interactions in the near wall region can enhance the local heat transfer at the wall more for one cylinder array than for the other at a Reynolds number. The effects are illustrated by the heat transfer results from the measurements presented later. The evolution of the region of negative v_x^* values with *t** downstream of the cylinder in Figs. 12 and 14 is caused by the flow reversal. The size of the negative v_x^* region is larger for the larger cylinder. The flow reversal region contributes to the pressure drop along the flow.

The vortex shedding frequency or Strouhal number may also affect the heat transfer enhancement as the near wall turbulence and flow mixing downstream of the cylinder are dependent on the vortex shedding. Katopodes (2019) reported the Strouhal number (*St*) increased with the *Re* in a shear-free crossflow about the cylinder up to a certain critical value of *Re.* The *St* in the present channel flow is also dependent on the *Re* till the critical value of *Re*. The *St* changes little above the critical *Re* value. The implications of vortex shedding in the present channel are then that the heat transfer at the wall will increase with the Reynolds number till the *Re* nears the critical value. The heat transfer enhancement at the wall will be primarily due to the flow accelerations at high Reynolds numbers beyond the critical *Re.*

6.2. Wall heat transfer (experiments)

The time-averaged heat transfer rate at the channel wall is quantified by the Nusselt number (*Nu*) defined in Eq. (2). The Nusselt numbers are estimated with the average heat flux at the wall and for the channel height, H = 5 mm. Figure 15 presents the distributions of local Nu_x along the channel as the *Re* varies for the staggered cylinder array of (d/p = 0.025, θ = 90°). The relative locations of the cylinders are also shown along the x/H-axis of the plot. The Nu_x values decrease from the channel inlet (x/H = 0) to the location of about x/H = 20 because of

the flow development. At $x/H > 20$, the periodic pattern of Nu_x is caused by the fully developed flow and local flow physics near the wall explained by the numerical results. The peaks in Nu_x for Re = 4000 and 9700 in Fig. 15 are caused by the flow accelerations and secondary flow interactions corresponding to the locations of the cylinders. The decelerating flow and reduction in the secondary flow interactions cause the Nu_x to decrease downstream of the cylinder central regions. Note, the cylinder locations are shown in pairs along x/H in the figure. Each pair represents the two cylinders in one staggered pattern. The peaks for the Nu_x data for Re = 920 in Fig. 15 are not distinguishable because of the low values and the Nu_x-scale used on the vertical axis. The Nu_x distributions increase with the Re at any x/H location because of the increase in the local mass flux and secondary flow interactions near the wall.

The local Nusselt numbers in the fully developed region between $50 < x/H < 90$ are averaged arithmetically for all the cylinder arrays and then presented in Figs. 16 and 17 with the Reynolds number. The average Nu_{avg} values in Fig. 16 are estimated for the staggered and in-line cylinder arrays with $\theta = 90°$. The average Nu_{avg} values in Fig. 17 are estimated for the cylinder arrays with $\theta = 45°$. The smooth channel Nusselt number data in the figures are obtained from the measurements of local data in a smooth channel with height H = 5 mm. In both the figures, Nu_{avg} values increase with Re and are higher for the cylinder arrays than for the smooth channel. There are no secondary flows and local acceleration of flow in the smooth channel. As the local Nusselt number increases with the Reynolds number, the average Nu_{avg} also increases. As predicted by the numerical flow field results, the combined influences of local flow accelerations and secondary flow interactions near the wall are different for the different cylinder arrays as the Re changes. The Nu_{avg} distributions are different for the different cylinder arrays in Figs. 16 and 17. However, as the pitch distance between the cylinders increases for both the in-line arrays and staggered arrays, the combined influences of flow accelerations and secondary flow interactions near the wall decrease. The Nu_{avg} distribution for

a given cylinder diameter (*d)* thus reduces as the pitch or *d/p* increases in both Fig. 16 and 17. The data of *d/p* = 0.1 and 0.05 in Figs. 16 and 17 show the effects of cylinder diameter at a constant θ and pitch-spacing. As the diameter doubles from *d/p* = 0.05 to *d/p* = 0.1 in Fig. 16, the Nu_{avg} are smaller for *d/p* = 0.1 than for *d/p* = 0.05 at *Re* > 3000. In Fig. 17, the Nu_{avg} are higher for *d/p* = 0.1 than for *d/p* = 0.05 at *Re* > 3000. The effects of the cylinder diameter on Nu_{avg} are primarily caused by the local flow accelerations in the gap between the cylinder and channel wall. The comparisons between Fig. 16 and 17 show slight decrease in the Nu_{avg} distributions as the θ changes from 90° to 45°. The results of Eiamsa-Ard and Promvonge (2009) with the triangular rib-groove combination and Vujicic (1994) with the cylinder array are compared with present data in Fig. 16. The present data are higher than those in Vujicic (1994). The smooth channel data from Marco and Han (1955) and Gnielinski (1976) are included in Fig. 17 to provide a qualification check for the present test methods.

The ratio of average Nusselt number (Nu_{avg}) for a cylinder array to fully developed Nusselt number (Nu_0) for the smooth channel quantifies the enhancement of convective heat transfer for the cylinder array. A value of (Nu_{avg}/Nu_0) > 1.0 is thus desirable. The ratios, Nu_{avg}/Nu_0 are determined from the data presented in Figs. 16 and 17 and are presented for all the test cases in Figs. 18 and 19. The data in Fig. 18 are shown for θ = 90° and in Fig. 19 for θ = 45°. The Nu_{avg}/Nu_0 values in both figures increase with *Re* till the *Re* value reaches about 3000. At *Re* > 3000, the Nu_{avg}/Nu_0 values decrease as *Re* increases irrespective of the cylinder array configuration in both Fig. 18 and 19. However, the Nu_{avg}/Nu_0 values are more sensitive to the change in *Re* at *Re* < 3000 than at *Re* > 3000 as the Nu_{avg}/Nu_0 value for a cylinder array increases by larger amount only for a ΔRe = (3000-640) = 2360 at *Re* < 3000. The effects of vortex shedding frequency on the near wall flow structure increase with *Re* in the low Reynolds number range, but become almost constant in the high Reynolds number range when the Strouhal number of the vortex shedding change little as explained in the numerical result

section. The effects are combined with the effects of local flow accelerations at all Reynolds numbers. The Nu_{avg}/Nu_0 values thus increase with $Re < 3000$. In the high Reynolds number range, the Nu_{avg} for the cylinder array increases as the mass flux near the heated wall increases with *Re*, much like the increase in Nu_0 with *Re* in the smooth channel. The Nu_{avg}/Nu_0 values thus decrease in the range of $Re > 3000$, but remain greater than 1.0. The Nu_{avg}/Nu_0 values in Figs. 18 and 19 are generally the highest for the cases ($\theta = 90°, 45°$) of in-line array with $d/p = 0.2$. The lowest Nu_{avg}/Nu_0 values in the figures are reported for the cases ($\theta = 90°, 45°$) of staggered array with $d/p = 0.025$. As the d/p decreases from 0.2 to 0.1 for the in-line array and from 0.05 to 0.025 for the staggered array, the Nu_{avg}/Nu_0 ratios generally decrease at all $Re > 3000$ irrespective of the angle (θ). The qualitative effects of d/p and *Re* are thus opposite to each other at $Re > 3000$. The effects of d/p on Nu_{avg}/Nu_0 ratios are much smaller at $Re < 3000$ compared to those at $Re > 3000$ in both Fig. 18 and 19. Also, the comparisons between Fig. 18 and 19 show small differences in the Nu_{avg}/Nu_0 distributions as the θ changes. The Nusselt number ratios for some references such as Eiamsa-Ard and Promvonge (2009), Eren and Caliskan (2016), and Tang and Zhu (2012) are included in Fig. 18 for comparisons. The data of the references were obtained with the internal fins, grooves and ribs in the channel wall, but not with the inserts.

Three functional relationships between the experimental Nu_{avg} and (*Re, d/p,* θ*, staggered, in-line*) are presented as correlations in Eqs. (8-10). Figure 20 shows the comparisons of data between the experiments and correlation equations. Most of the calculated $\left(\frac{Nu}{\theta^{6r}}\right)$, $\left(\frac{Nu}{\theta^{0.8r}}\right)$, and $\left(\frac{Nu}{\theta^{3r}}\right)$ values from the correlations fall within the ±15% bounds of the experimental values in Fig. 20. The deviations of the calculated values in Fig. 20(c) outside the ±15% bounds occur when $Re > 1800$.

For staggered, $600 < Re < 13{,}000$, $r = d/p = (0.025, 0.05)$, $\theta = (\pi/4, \pi/2)$:

$$\left(\frac{Nu}{\theta^{6r}}\right) = 0.201(Re)^{0.5902} \quad (8)$$

For in-line, 600 < *Re* < 13,000, $r = d/p$ = (0.1, 0.2), θ = (π/4, π/2):

$$\left(\frac{Nu}{\theta^{0.8r}}\right) = 0.2322(Re)^{0.5911} \quad (9)$$

For staggered and in-line, 600 < *Re* < 13,000, $r = d/p$ = (0.025 - 0.2), θ = (π/4, π/2):

$$\left(\frac{Nu}{\theta^{3r}}\right) = 0.2174(Re)^{0.5833} \quad (10)$$

6.3. Pressure drop (experiments)

The results of pressure drop measurements in the test channel is reported as the friction factor (*f*) in Figs. 21 and 22 for the cylinder arrays with θ = 90° and θ = 45°, respectively. The channel height for the results is H = 5 mm. The results in a smooth channel without any cylinders are also included in Fig. 21. The friction factor (*f*) is calculated in Eq. (11) from the measured pressure drop ΔP_x along the channel. The measured pressure distributions in the fully developed flow section are used to determine the $\Delta P_x/\Delta x$ for Eq. (11) as explained in Mahmood et al. (2015).

$$f = \frac{(\Delta P_x/\Delta x)(D_h/4)}{(1/2)\rho V_{avg}^2} \quad (11)$$

Figure 21 and Figure 22 show the friction factors (*f*) for all the cylinder arrays decrease sharply as the *Re* increases until *Re* nears the value of 5000. The distributions of *f* at *Re* > 5000 become almost constant. With the decrease in *d/p* from 0.2 to 0.1 for the in-line array and from 0.05 to 0.025 for the staggered array, the *f* values decrease irrespective of the *Re* and θ in both figures. The numerical results presented earlier show the very weak interactions of vortices between two consecutive cylinders in an array. As the pitch-spacing (*p*) between the cylinders is increased for a constant diameter (*d*), the wakes from a cylinder affect the wakes from the downstream cylinder negligibly. Consequently, the ΔP_x and friction factor decrease when the *d/p* deceases at a constant diameter in Figs. 21 and 22. The cylinder arrays with *d/p* = 0.2

provides the largest distributions of f. The lowest values of f among the cylinder arrays are reported for the cases (θ = 90°, 45°) of staggered array with d/p = 0.025. The comparisons between Fig. 21 and Fig. 22 show the f distributions decrease as the θ changes from 90° to 45°. The effects of θ are thus more pronounced for the friction factors than for the average Nusselt numbers. The results of the numerical flow field show locally convoluted streamlines deviating from the parallel direction to the channel walls with presence of cylinders. The friction factors in Figs. 21 and 22 are thus higher for the cylinder arrays than for the smooth channel. The effects of cylinder diameter on the f can be seen when the d/p = 0.1 case is compared with the d/p = 0.05 case in Figs. 21 and 22. The pitch-spacing is the same for both cases as the θ remains constant. The f distributions change little the dimeter doubles. The data from Eiamsa-Ard and Promvonge (2009) for rib-grooves are presented in Fig. 21. The experimental friction factors in smooth channel in Fig. 22 compare very well with the smooth channel friction factors obtained from the equations in Shah and London (1978) and Kármán-Nikuradse (Kays and Crawford, 1993). The maximum difference between the correlation and experimental friction factor for the smooth channel is 8% for Re < 2800 and 5% for Re > 2800.

The friction factor ratios (f/f_0) vs. Re are plotted in Fig. 23 and Fig. 24 for θ = 90° and θ = 45°, respectively, for all the cylinder arrays. The increase in pressure drop across the channel for a cylinder array relative to the pressure drop in a smooth channel without any cylinders is provided by the ratio, f/f_0. The experimental friction factors (f) for the cylinder array and measured friction factors (f_0) for the smooth channel from Figs. 21 and 22 are used to estimate the ratio, f/f_0. As shown in Figs. 23 and 24, the f/f_0 ratios increase sharply with the Re when Re < 2000. The f/f_0 ratios change little as the Re changes at Re > 2000. Also, the decrease in d/p causes the decrease in f and f/f_0. The d/p = 0.2 case on in-line arrays provide the highest f/f_0 distributions in both Figs. 23 and 24. The ratios are the lowest for the d/p = 0.025 of staggered cases among the cylinder arrays in both figures. The data for θ = 90° in Fig. 23 are compared

with the friction factor ratios from Eiamsa-ard and Promvonge (2009), Eren and Caliskan (2016) and Tang and Zhu (2012) dealing with rib-grooves and pin-fins. The data of Eiamsa-ard and Promvonge (2009) are much smaller than those for the cylinder arrays in Fig. 23.

Three functional relationships between the experimental *f* and (*Re, d/p, θ, staggered, in-line*) are presented as correlations in Eqs. (12-14). Figure 25 shows the comparisons of data between the experiments and correlation equations. Most of the calculated values of $\left[Ln\left(\frac{1}{f}+1\right)\right]_{correl}$ from the correlations fall within the ±15% bounds of the experimental values in Fig. 25. The deviations of the calculated values in Figs. 25(a, b) beyond the ±15% bounds occur when *Re* > 5000. The calculated values in Fig. 25(c) are also outside the ±15% bounds for the in-line case of (*d/p* = 0.2, θ = 90°) and staggered case of (*d/p* = 0.025, θ = 45°). The very high values of friction factors due to small pitch in the in-line case of (*d/p* = 0.2, θ = 90°) and the low values of friction factors due to high pitch in the staggered case of (*d/p* = 0.025, θ = 45°) cause the high deviations in the calculated values.

For staggered, 600 < *Re* < 13,000, *r* = *d/p* = (0.025, 0.05), θ = (π/4, π/2):

$$Ln\left(\frac{1}{f}+1\right) = 0.1968 + 0.3482\ Ln(Re) - 2r\ Ln(\theta) \tag{12}$$

For in-line, 600 < *Re* < 13,000, *r* = *d/p* = (0.1, 0.2), θ = (π/4, π/2):

$$Ln\left(\frac{1}{f}+1\right) = -0.1207 + 0.3216\ Ln(Re) - 2r\ Ln(\theta) \tag{13}$$

For staggered and in-line, 600 < *Re* < 13,000, *r* = *d/p* = (0.025 - 0.2), θ = (π/4, π/2):

$$Ln\left(\frac{1}{f}+1\right) = -0.0988 + 0.3531\ Ln(Re) - 2r\ Ln(\theta) \tag{14}$$

6.4. Thermal performance (experiments)

The thermal performance coefficient (η) defined in Eq. (15) based on Gee and Webb (1980) and Webb and Eckert (1972) are presented in Figs. 26 and 27 for θ = 90° and θ = 45°,

respectively. The coefficient quantifies the enhancement of heat transfer as the pressure penalty in the channel increases. A value of $\eta > 1.0$ is desirable for the increase in heat transfer rate without the increase in pumping power and surface area or for the decrease in heat transfer area without the decrease in heat transfer and pumping power. As indicated in both Fig. 26 and Fig. 27, the thermal performance coefficients increase with the *Re* at *Re* < 3000 and decrease as the *Re* increases at *Re* > 3000. The largest η is provided by the staggered cylinder array with *d/p* = 0.025 at *Re* = 3000 in both figures. The $\eta \geq 1.0$ values are obtained between *Re* = 920 and *Re* = 7000 for all the cylinder arrays. The differences in η distributions are small between the cylinder arrays as the *d/p* and θ change at a constant Reynolds number.

$$\eta = \frac{\frac{Nu}{Nu_0}}{\left(\frac{f}{f_0}\right)^{\frac{1}{3}}} \tag{15}$$

7. Conclusions

Numerical simulations of the flow and measurements of the pressure drop and wall heat transfer are performed in a rectangular channel employing eight different arrays of cylindrical rods as inserts. The effects of cylinder array and Reynolds number on the pressure drop and heat transfer rate are investigated. Some correlations are provided for the Nusselt numbers and friction factors. The novelties of the investigations are in the employment of limiting pressure-enhancing cylindrical bars as the heat transfer enhancing inserts in the channel flow, the simple and cheap construction of the cylinder array, and the applicability of the cylinder arrays over a wide range of the Reynolds numbers. The results are summarized in the following.

- Numerical results show local flow accelerates in the gap between cylinder and channel wall. The vortex shedding downstream of a cylinder interacts with the near wall turbulent flow and causes deviations in streamlines from the main flow direction.
- The average Nusselt number, friction factor, and thermal performance coefficient are affected by the Reynolds number and cylinder array diameter-to-pitch ratio. The effects

of the cylinder orientation relative to the main flow on the Nusselt number and friction factor are the minimum.

- At a constant pitch-spacing in the cylinder array, the effects of cylinder diameter on the Nusselt number are significant. However, the effects of cylinder diameter on the friction factor are insignificant.
- The ratio of cylinder array Nusselt number to smooth channel Nusselt number increases with the Reynolds number (*Re*) when the $Re < 3000$ and decreases as the *Re* increases when $Re > 3000$. The ratio of Nusselt number is always higher at the higher diameter-to-pitch ratio of the cylinder array.
- The ratio of cylinder array friction factor to smooth channel friction factor increases with the Reynolds number (*Re*) when the $Re < 3000$ and changes little with the *Re* when $Re > 3000$. The ratio of friction factor is also always higher at the higher diameter-to-pitch ratio of the cylinder array similar to the Nusselt number ratio.
- The thermal performance coefficient increases with the Reynolds number (*Re*) when the $Re < 3000$ and decreases as the *Re* increases when $Re > 3000$. The desirable value of the performance coefficient at 1.0 and larger than 1.0 are obtained when the Reynolds number ranges between 1000 and 7000 irrespective of the cylinder array geometry. The thermal performance parameter is not much sensitive to the diameter-to-pitch ratio of the array at the cylinder orientation of 90°. However, the thermal performance at the cylinder orientation of 45° decreases as the diameter-to-pitch ratio increases.

Acknowledgment

The authors are grateful to Chris Govinder and Donald Keetse for their assistance in the test setup.

Conflict of interests

None.

Table 1: Details of cylinder arrays with channel height, H = 5 mm.

d (**mm**)	**p** (**mm**)	**θ**	**d/p**	**Staggered/In-line**
1	40	90°	0.025	Staggered
1	40	45°	0.025	Staggered
1 or 5*	20 or 100*	90°	0.05	Staggered*
1	20	45°	0.05	Staggered
2	20	90°	0.1	Inline
2	20	45°	0.1	Inline
2 or 10*	10 or 50*	90°	0.2	Inline*
2	10	45°	0.2	Inline

*(d = 5 mm, p = 100 mm) and (d = 10 mm, p = 50 mm) at H = 25 mm test cases are used for numerical model validation.

Nomenclature

A_c	Cross-sectional area of test section, [m^2]
d, D_h	Cylinder diameter and Hydraulic diameter , [m]
f, f_0	Friction factor: cylinder array and smooth channel
H, L, W	Height, length, and width of channel, [m]
$C_{p,a}, k_a$	Air property: specific heat at constant pressure [J/kg.K], and thermal conductivity, [W/m.K]
$\dot{m}$	Air mass flow rate, $(\rho\, V_{avg}\, A_c)$, [kg/s]
Nu_0	Fully-developed Nusselt number in smooth channel
Nu_x, Nu_{avg}	Nusselt number: local along channel wall and average of local
P_x, P_α	Static pressure: on channel surface and on cylinder surface, [Pa]
p	Pitch-space between cylinders, [m]
Q_c	Convective heat transfer rate, [W]
Re	Reynolds number, $(\dot{m}D_h/\mu A_c)$
$T_{a,x=0}$	Flow temperature at test section inlet, [°C]
$T_{w,x}, T_{m,x}$	Local temperature: on heater surface and mixed-mean of air, [°C]
t, t^*	Time: dimensional, [s], and non-dimensional
$U_{H/2}, U_{H/4}$	Local time-averaged velocity along x direction, [m/s]
V_{avg}	Time and mass-averaged velocity in channel, [m/s]
v_x, v_x^*	Steamwise time-dependent velocity: dimensional, [m/s], and non-dimensional
x, y, z	Local Cartesian coordinates

Greek symbols

α	*Angle around rod*
Δ	Difference in quantity

η	Thermal performance coefficient
θ	Cylinder angle with flow direction
μ, ρ	Air viscosity and density
ω_z, ω_z^*	z-vorticity component: dimensional, non-dimensional

References

Aharwal, K.R., Pawar C.B., and Chaube, A., Heat transfer and fluid flow analysis of artificially roughened ducts having rib and groove roughness, *Heat Mass Transf.*, vol. **50**, pp. 835-847, 2014. https://doi.org/10.1007/s00231-014-1292-6.

Apsley, D. and Leschziner, M., Advanced turbulence modelling of seperated flow in a diffuser. *Flow, Turbulence Combustions*, vol. **63**, pp. 81-112, 2000. https://doi.org/10.1023/A:1009930107544.

Beckwith, T.G., Marangoni, R.D., and Lienhard, J.H., *Mechanical Measurements*, sixth ed. Pearson Prentice Hall, New Jersey, pp. 42-45, 54-59, 2007.

Cramer, L., Enhancement of the Thermal Performance of Solar Heat Exchanges with Porous Inserts, M.Eng. thesis, University of Pretoria, 2018.

Eiamsa-Ard, S., Nanan, K., Wongcharee, K., Yongsiri, K., and Thiapong, C., Thermohydraulic Performance of Heat Exchanger Tube Equipped with Single-, Double-, and Triple-Helical Twisted Tapes, *Chem. Eng. Commu.*, vol. **202**, pp. 606-615, 2015. https://doi.org/10.1080/00986445.2013.858038.

Eiamsa-Ard, S. and Promvonge, P., Thermal characteristics of turbulent rib-grooved channel flows, *Int. Commun. Heat Mass Transf.*, vol. **36**, 705-711, 2009.

https://doi.org/10.1016/j.icheatmasstransfer.2009.03.025.

Eren, N. and Caliskan, S., Effect of grooved pin-fins in a rectangular channel on heat transfer augmentation and friction factor using Taguchi method, Int. *J. Heat Mass Transf*., vol. **102**, pp. 1108-1122, 2016. https://doi.org/10.2298/TSCI180421306B.

Fiebig, M., Valencia, A., and Mitra, N., Local heat transfer and flow losses in fin-and-tube heat exchangers with vortex generators: A comparison of round and flat tubes, *Exp. Thermal Fluid Science*, vol. **8**, pp. 35-45, 1994. https://doi.org/10.1016/0894-1777(94)90071-X.

Gee, D.L. and Webb, R.L.,Forced convection heat transfer in helically rib-roughened tubes, *Int. J. Heat Mass Transfer*, vol. **23**, pp. 1127-1136, 1980. https://doi.org/10.1016/0017-9310(80)90177-5.

Gnielinski, V., New equations for heat and mass transfer in turbulent pipe and channel flow, *Int. Chemical Eng*., vol. **16**, no. 2, pp. 359-368, 1976.

International Standard, Measurement of Fluid Flow by Means of Orifice Plates, Nozzles and Venture Tubes Inserted in Circular Cross-Section Conduits Running Full, *International Organization for Standardization*, ISO 5167-1:1991.

Jamalabadi, M.Y.A. and Oveisi, M., Numerical simulation of interaction of a current with a circular cylinder near a rigid bed, *J. Applied Math. Phys.*, vol. **4**, pp. 398-411, 2016. http://dx.doi.org/10.4236/jamp.2016.42047.

Katopodes, N.D., *Free Surface Flow: Environmental Fluid Mechanics*, Butterworth-Heinemann (Elsevier), Chap. 5, pp. 324-426, 2019. https://doi.org/10.1016/B978-0-12-815489-2.00005-8.

Kays, W.M. and Crawford, M.E, *Convective Heat and Mass Transfer*, third ed., McGraw-Hill, Inc., printed in USA, pp. 249, 1993.

Kumar, A. and Layek, A., Nusselt number-friction characteristic for a twisted rib roughened rectangular duct using liquid crystal thermography, *Exp. Thermal Fluid Science.*, vol. **97**, pp. 205-217, 2018. https://doi.org/10.1016/j.expthermflusci.2018.04.017.

Leonardi, S., Orlandi, P., Djenidi, L., and Antonie, R., Heat transfer in a turbulent channel flow with square bars or circular rods on one wall, *J. Fluid Mech.*, vol. **776**, pp. 512-530, 2015. https://doi.org/10.1017/jfm.2015.344.

Li, X., Xie, G., Liu, J., and Sundén, B., Parametric study on flow characteristics and heat transfer in rectangular channels with strip slits in ribs on one wall, *Int. J. Heat Mass Transf.*, vol. **149**, pp. 118396, 2000. https://doi.org/10.1016/j.ijheatmasstransfer.2019.07.046.

Lotfi, B., Sundén, B., and Wang, Q., An investigation of the thermo-hydraulic performance of the smooth wavy fin-and-elliptical tube heat exchangers utilizing new type vortex generators, *Appl. Energ.*, vol. **162**, pp. 1282-1302, 2016. https://doi.org/10.1016/j.apenergy.2015.07.065.

Mahmood, G.I., Simonson, C.J., and Besant, R.W., Experimental pressure drop and heat transfer in a rectangular channel with a sinusoidal porous screen, *J. Heat Transfer,* vol. **137**, pp. 0426011-04260111, 2015. https://doi.org/10.1115/1.4029349.

Marco, S.M. and Han, L.S., A note on limiting laminar Nusselt number in ducts with constant temperature gradient by analogy to thin-plate theory, *ASME Trans.* **77**, no.5, pp. 625-630, 1955. https://doi.org/10.1115/1.4014446.

Menter, F.R., Two-equation eddy-viscosity turbulence models for engineering applications, *AIAA J.*, vol. **32**, pp. 1598-1605, 1994. https://doi.org/10.2514/3.12149.

Moffat, R.J., Descibing the uncertainty in experimental results, *Exp. Thermal Fluid Sc.*, vol. **1**, pp. 3-17, 1988. https://doi.org/10.1016/0894-1777(88)90043-X.

Mikic, B.B., Kapat, J., and Ratnathicam, J., Transition to turbulence in systems with eddy promoters: Implication for the question of transition, *Phys. Fluids*, vol. **4**, no.8, pp. 1854-1855, 1992. https://doi.org/10.1063/1.858357.

Sahu, M., Pandey, K., and Chatterjee, S., Thermo-hydraulic performance of rectangular channel roughened with combined semi-circular and triangular ribs, *Heat Mass Transfer*, vol. **55**, pp. 2889–2900, 2019. https://doi.org/10.1007/s00231-019-02630-0.

Salehi, M.A., Mazaheri, S., and Kazeminezhad, M.H., Study of flow characteristics around a near-wall circular cylinder subjected to a steady cross-flow, *Int. J. Coastal Offshore Eng.*, vol. **4**, pp. 45-55, 2018. DOI: 10.29252/ijcoe.1.4.45.

Sinha, A., Chattopadhyay, H., Iyengar A., and Biswas, G., Enhancement of heat transfer in a fin-tube heat exchanger using rectangular winglet type vortex generators, *Int. J. Heat Mass Transf.*, vol. **101**, pp. 667-681, 2016. https://doi.org/10.1016/j.ijheatmasstransfer.2016.05.032.

Shah, R.K. and London, A.L., *Laminar Flow Forced Convection in Ducts-A Source Book for Compact Heat Exchanger Analytical Data*, Academic Press Inc., New York, pp. 179-182, 1978.

Tang, X. and Zhu, D., Experimental and Numerical Study on Heat Transfer Enhancement of a Rectangular Channel with Discontinuous Crossed Ribs and Grooves, *Chinese J. Chemical Eng.*, vol. **20**, pp. 220-230, 2012. https://doi.org/10.1016/s1004-9541(12)60382-6.

Vujisic, L.B., Heat transfer at transition to turbulence in channel flows with eddy promoters, Ph.D. thesis, Massachusetts Inst. Tech., 1994. http://hdl.handle.net/1721.1/36499.

Webb, R.L. and Eckert, E.R.G., Application of rough surfaces to heat exchanger design, *Int. J. Heat Mass Transfer*, vol. **15**, pp. 1647-1658, 1972. https://doi.org/10.1016/0017-9310(72)90095-6.

Zheng, D., Wang, X., and Yuan, Q., The flow and heat transfer characteristics in a rectangular channel with convergent and divergent slit ribs, *Int. J. Heat Mass Transf.*, vol. **141**, pp. 464-475, 2019. https://doi.org/10.1016/j.ijheatmasstransfer.2019.06.060.

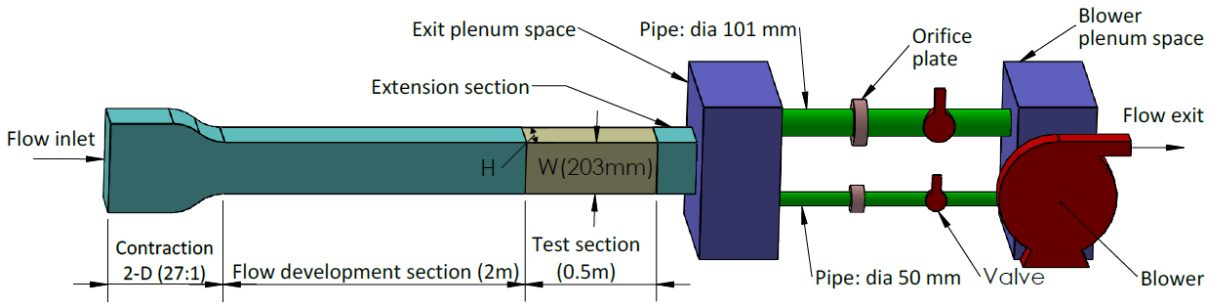

Figure 1. Schematic diagram of the experimental set-up. Channel height dimension H = 5.0 or 25 mm. “Pipe: dia” indicates the diameter of pipe.

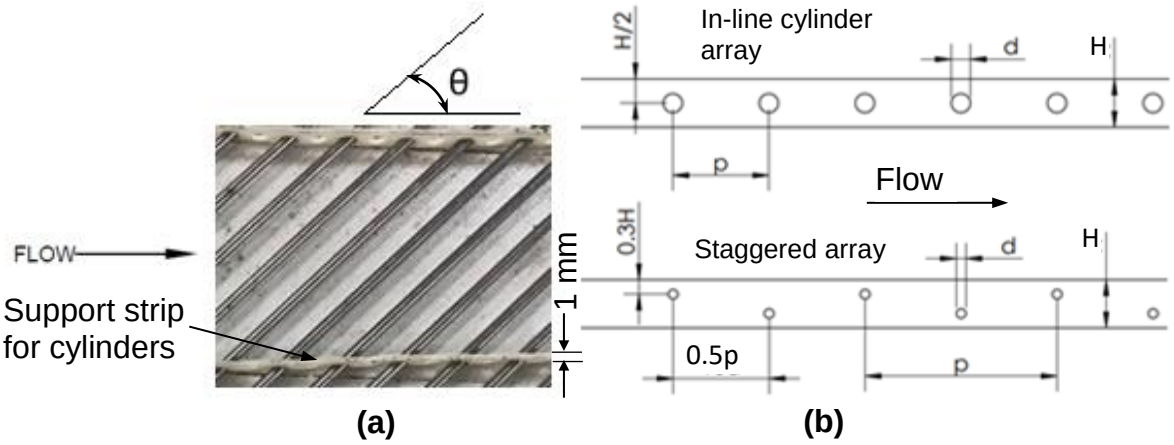

Figure 2. (a) Partial picture of an array of cylindrical cross-bars with d/p = 0.2, θ = 45°; (b) A schematic diagram of the placement of cylinders along test channel.

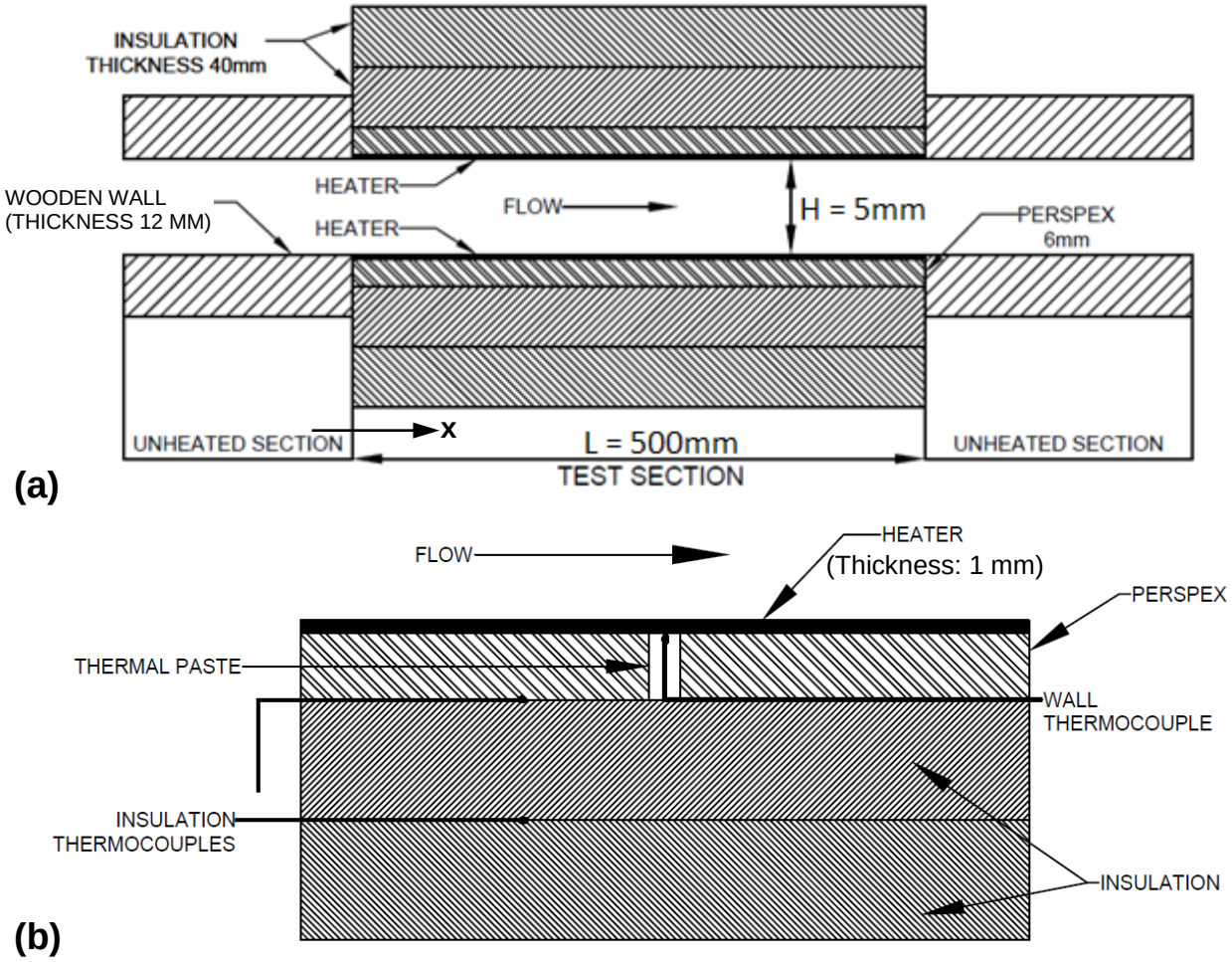

Figure 3. (a) Test section for heat transfer measurements; (b) Details of thermocouple installations in test section. Streamwise coordinate "x" originates at test section inlet (x = 0).

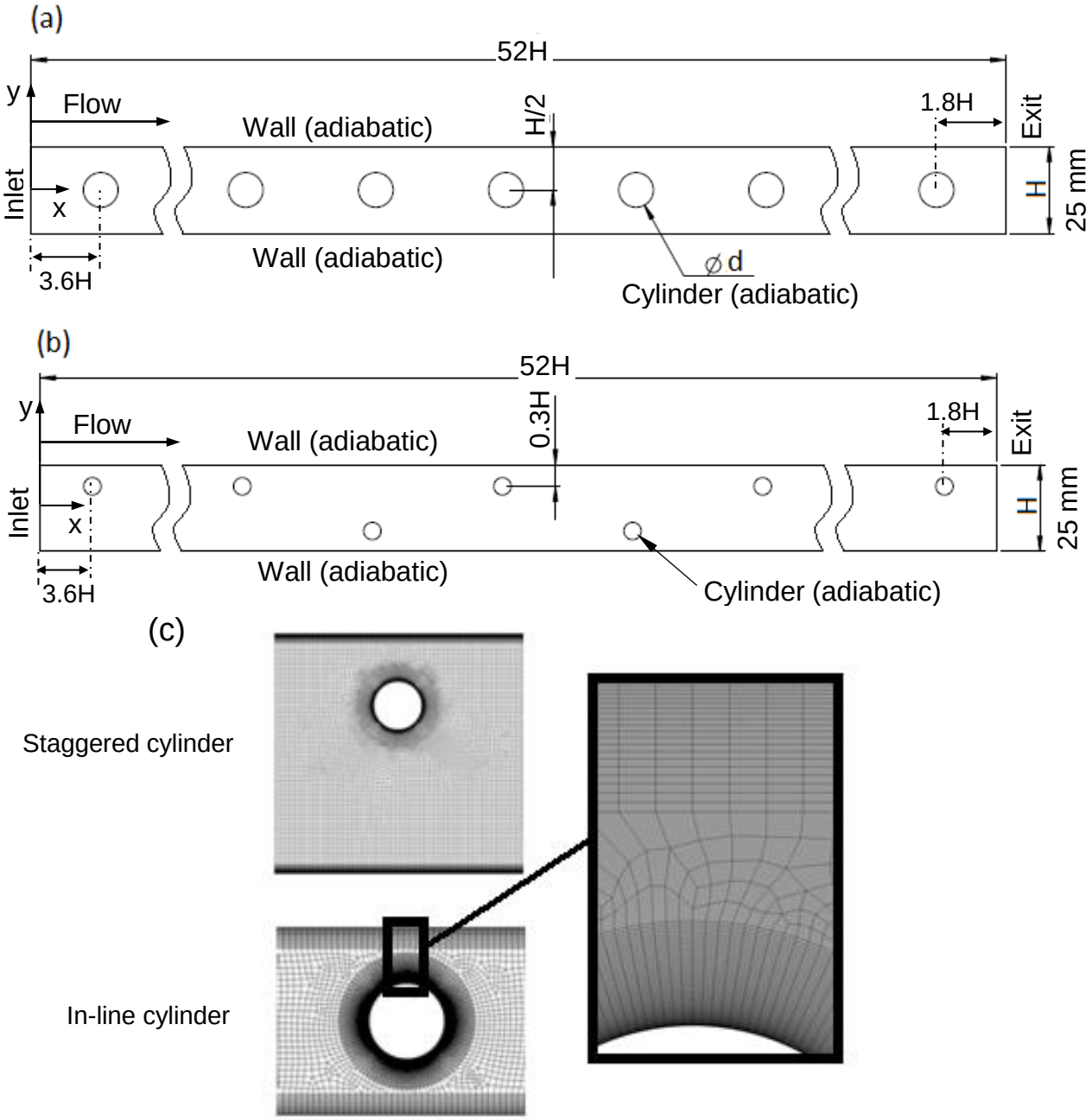

Figure 4. Geometry of numerical model: (a) d/p = 0.2, θ = 90°, d = 10 mm, in-line cylinder array (drawn not to scale); (b) d/p = 0.05, θ = 90°, d = 5 mm, staggered cylinder array (drawn not in scale); (c) Mesh details for staggered and in-line cylinder arrays.

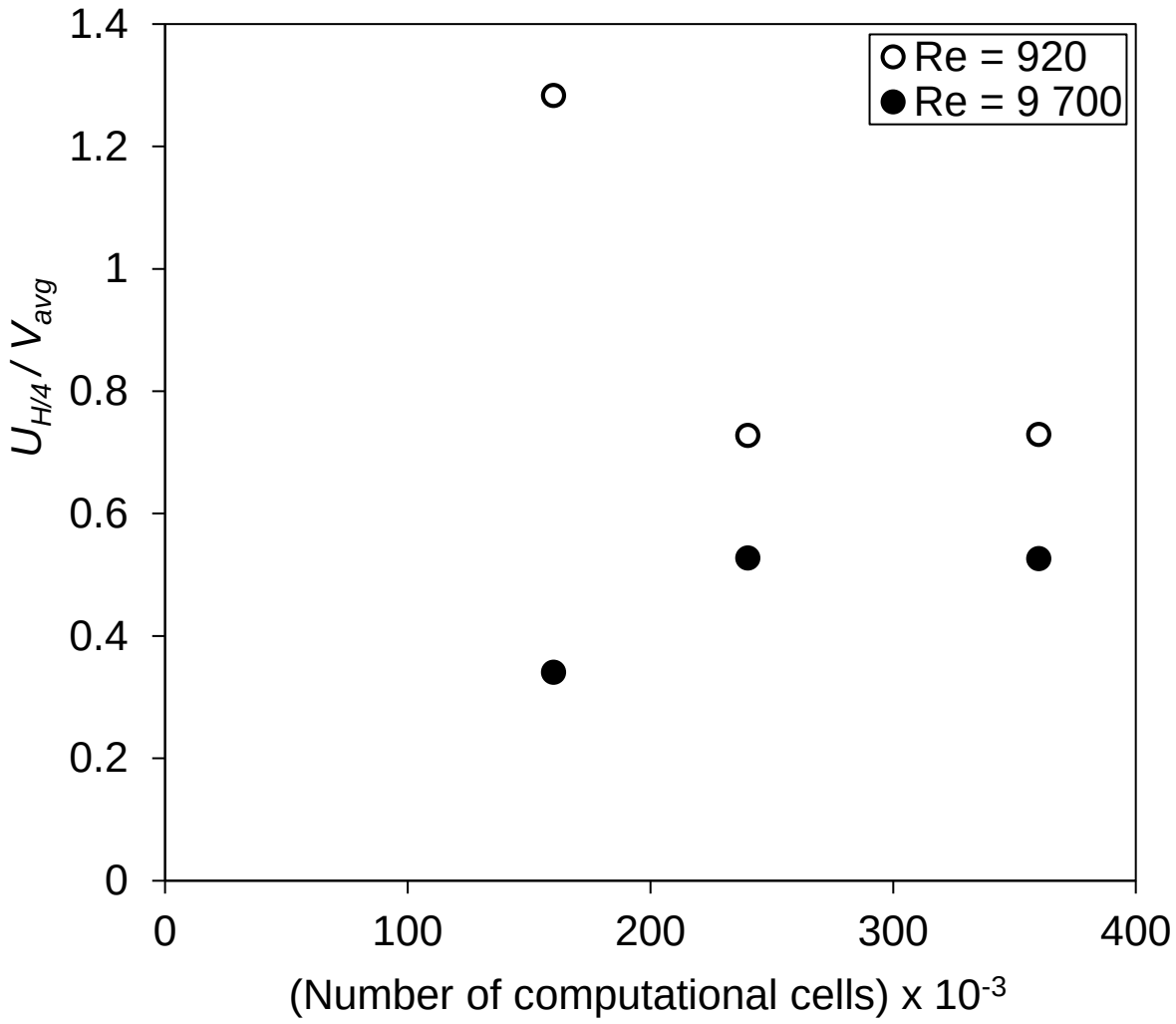

Figure 5. Normalized streamwise velocity, $U_{H/4}/V_{avg}$ at 2.5d downstream of the streamwise 5th cylinder and at H/4 distance from the top wall as the mesh number varies for the staggered cylinder array: d/p = 0.05, θ = 90°, d = 5 mm.

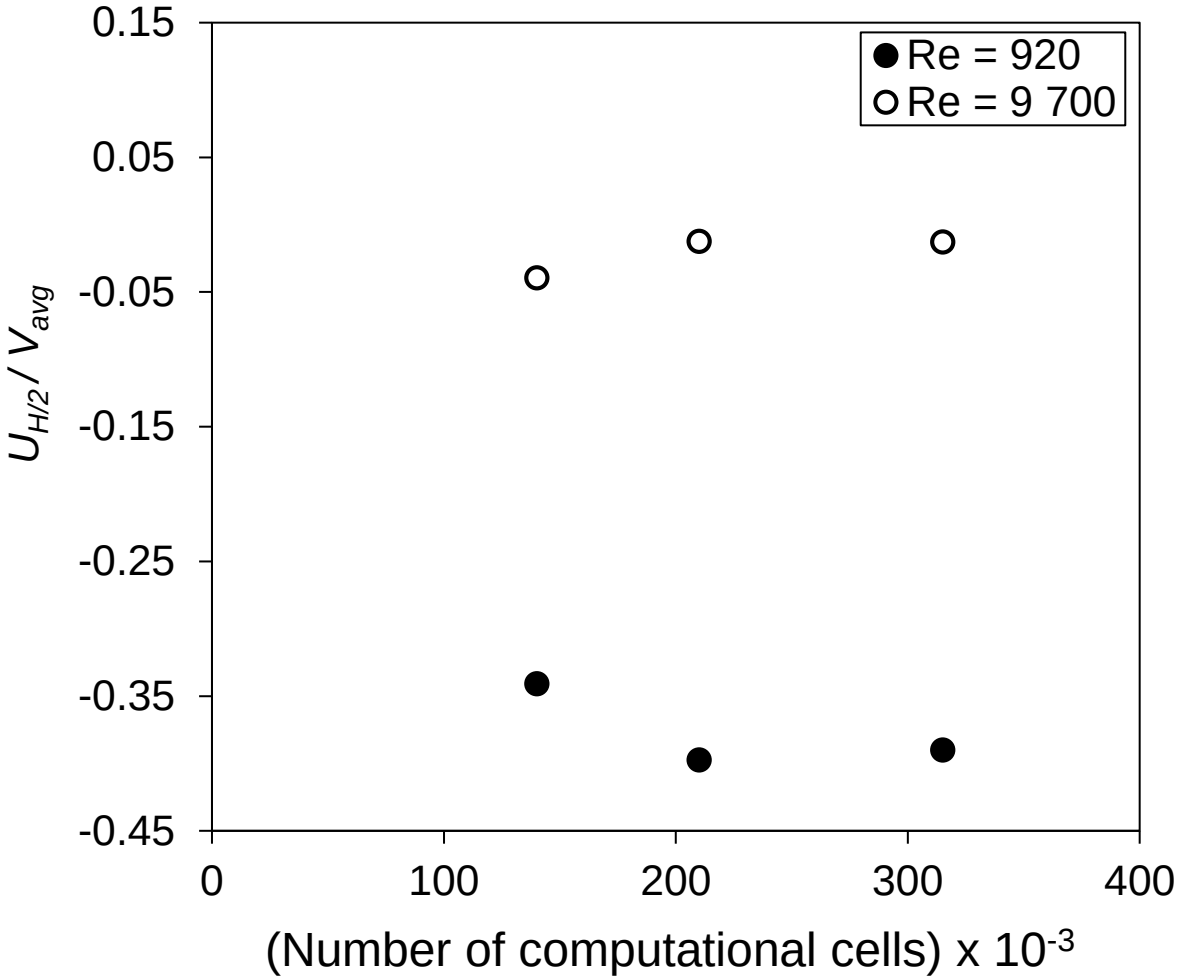

Figure 6. Normalized streamwise velocity, $U_{H/2}/V_{avg}$ at 2.5d downstream of the streamwise 5^{th} cylinder and at H/2 distance from the top wall as the mesh number varies for the in-line cylinder array: d/p = 0.2, θ = 90°, d = 10 mm.

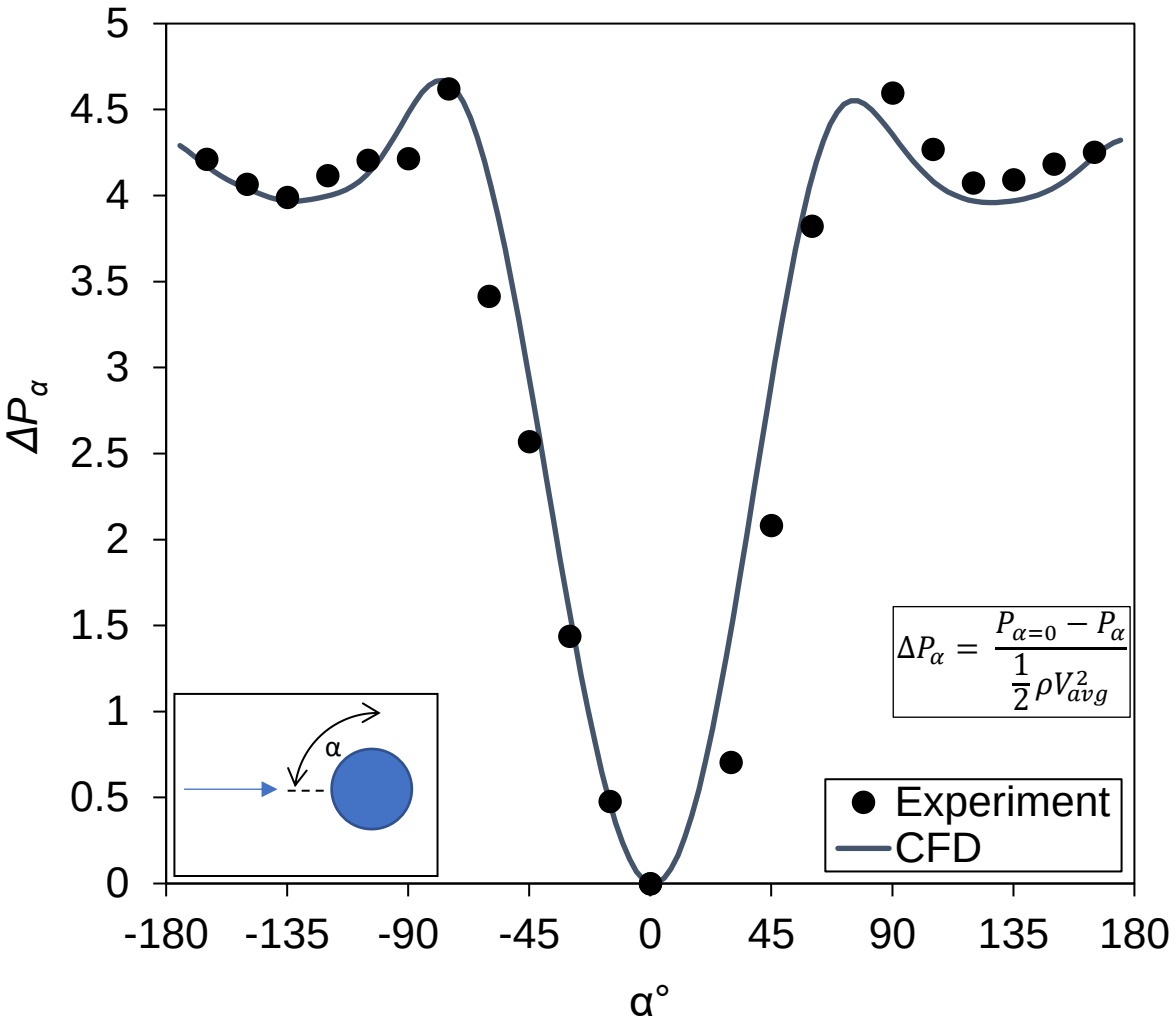

Figure 7. CFD model validation- Comparison of pressure coefficients, ΔP_α between numerical model (CFD) and experiment for the staggered array: $\theta = 90°$, $d/p = 0.05$, $d = 5$ mm, $Re = 9700$.

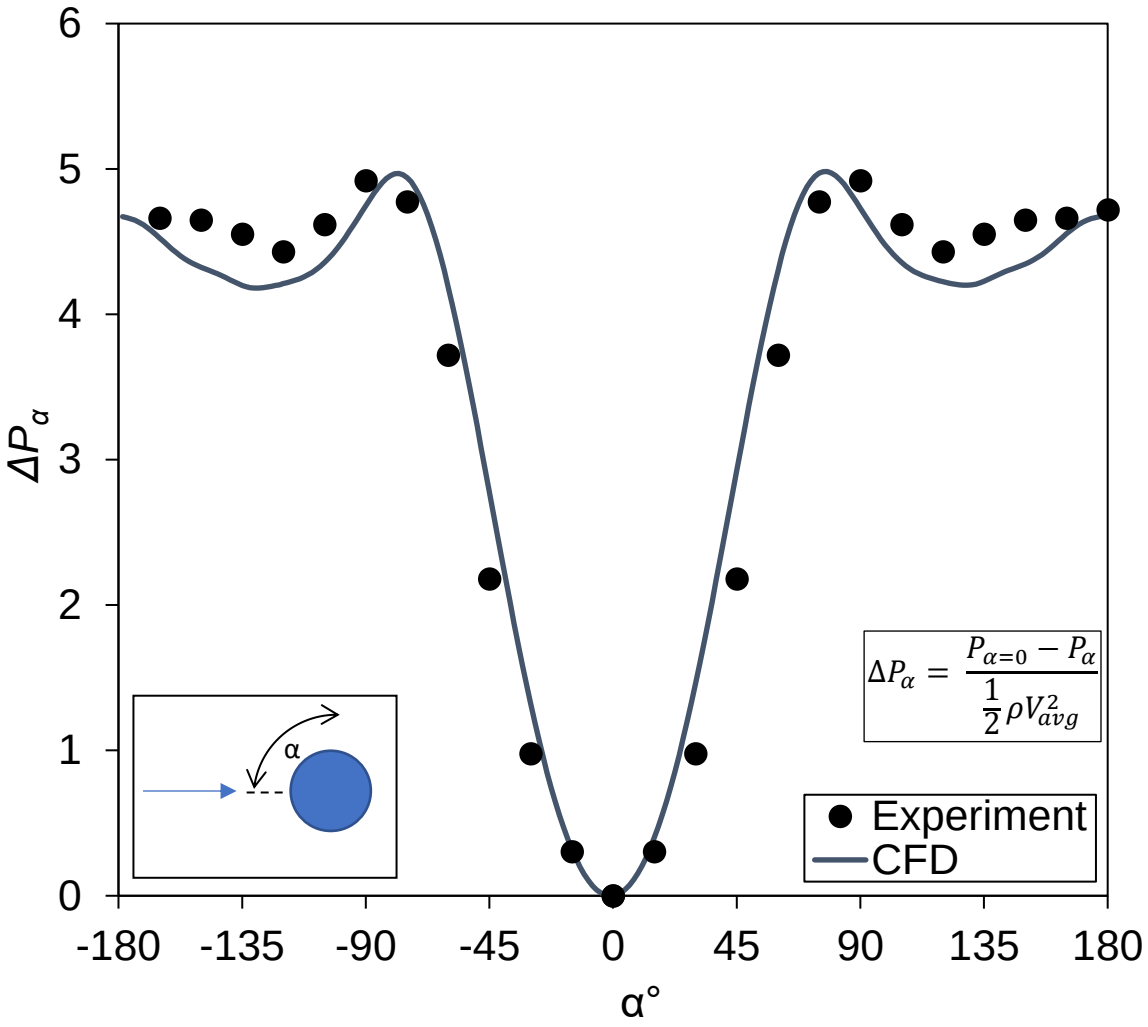

Figure 8. CFD model validation- Comparison of pressure coefficients, ΔP_α between numerical model (CFD) and experiment for the in-line array: θ = 90°, d/p = 0.2, d = 10 mm, Re = 9700.

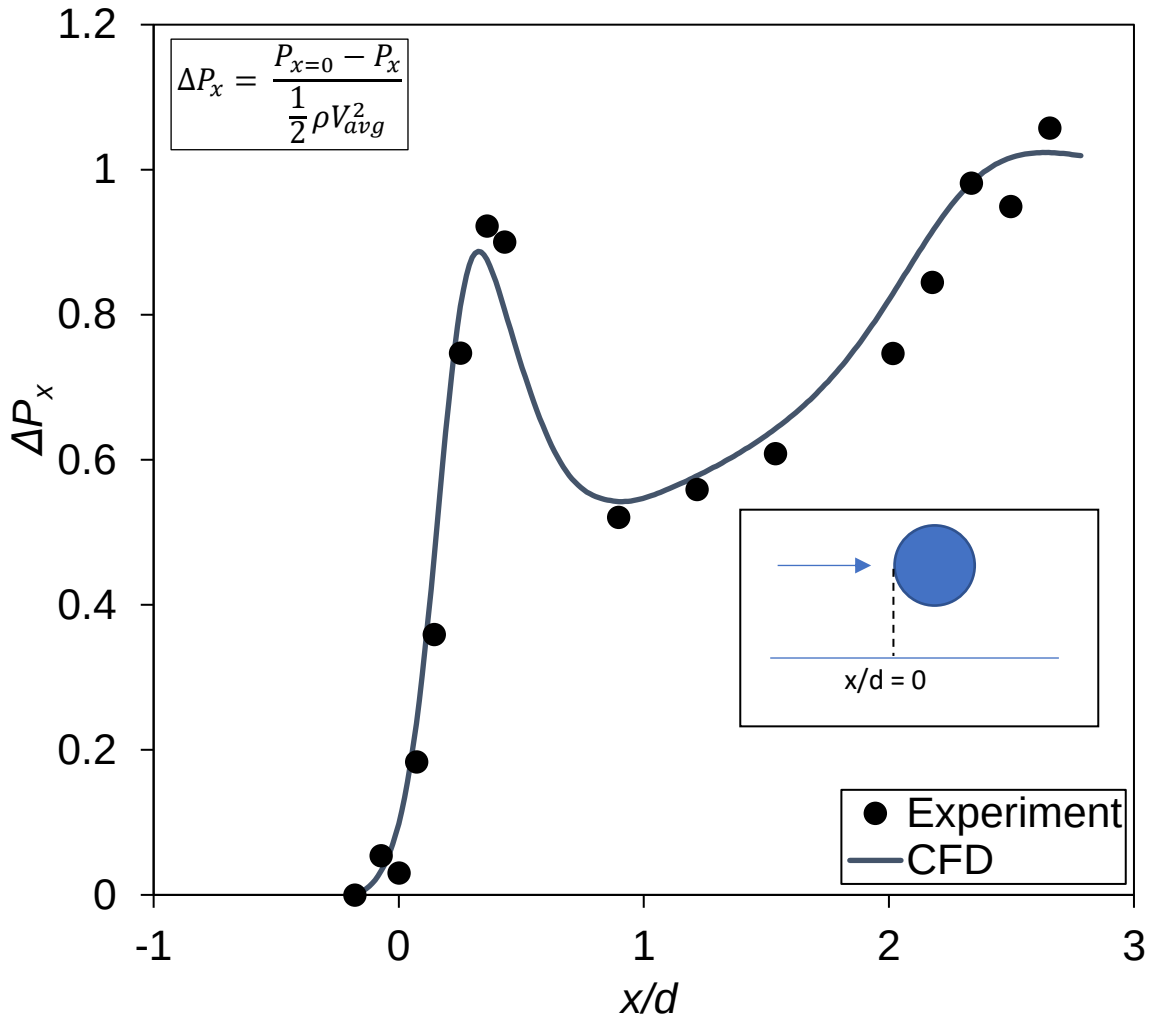

Figure 9. CFD model validation- Comparison of pressure coefficients, ΔP_x between numerical model (CFD) and experiment for the staggered array: θ = 90°, d/p = 0.05, d = 5 mm, Re = 9700.

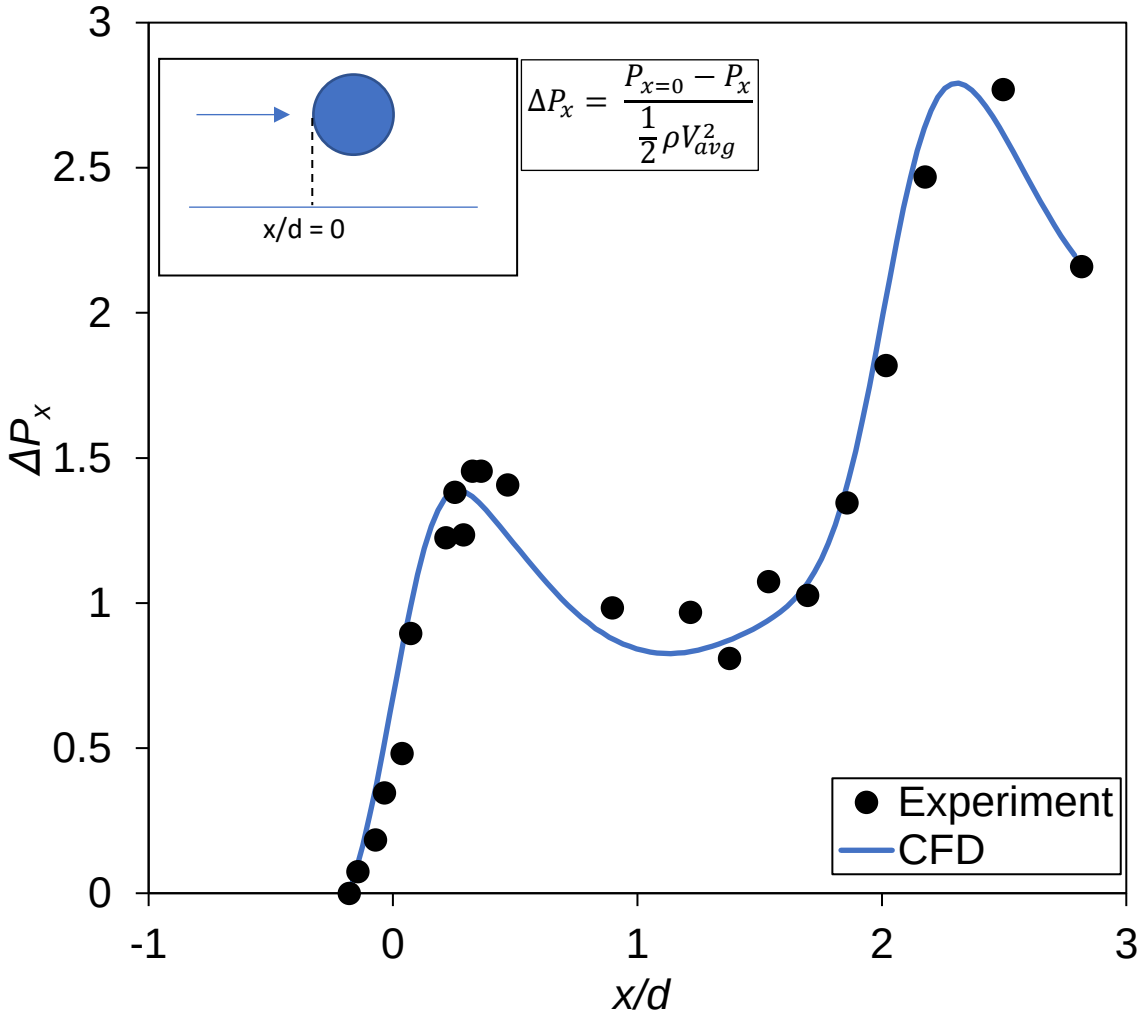

Figure 10. CFD model validation- Comparison of pressure coefficients, ΔP_x between numerical model (CFD) and experiment for the in-line array: θ = 90°, d/p = 0.2, d = 10 mm, Re = 9700.

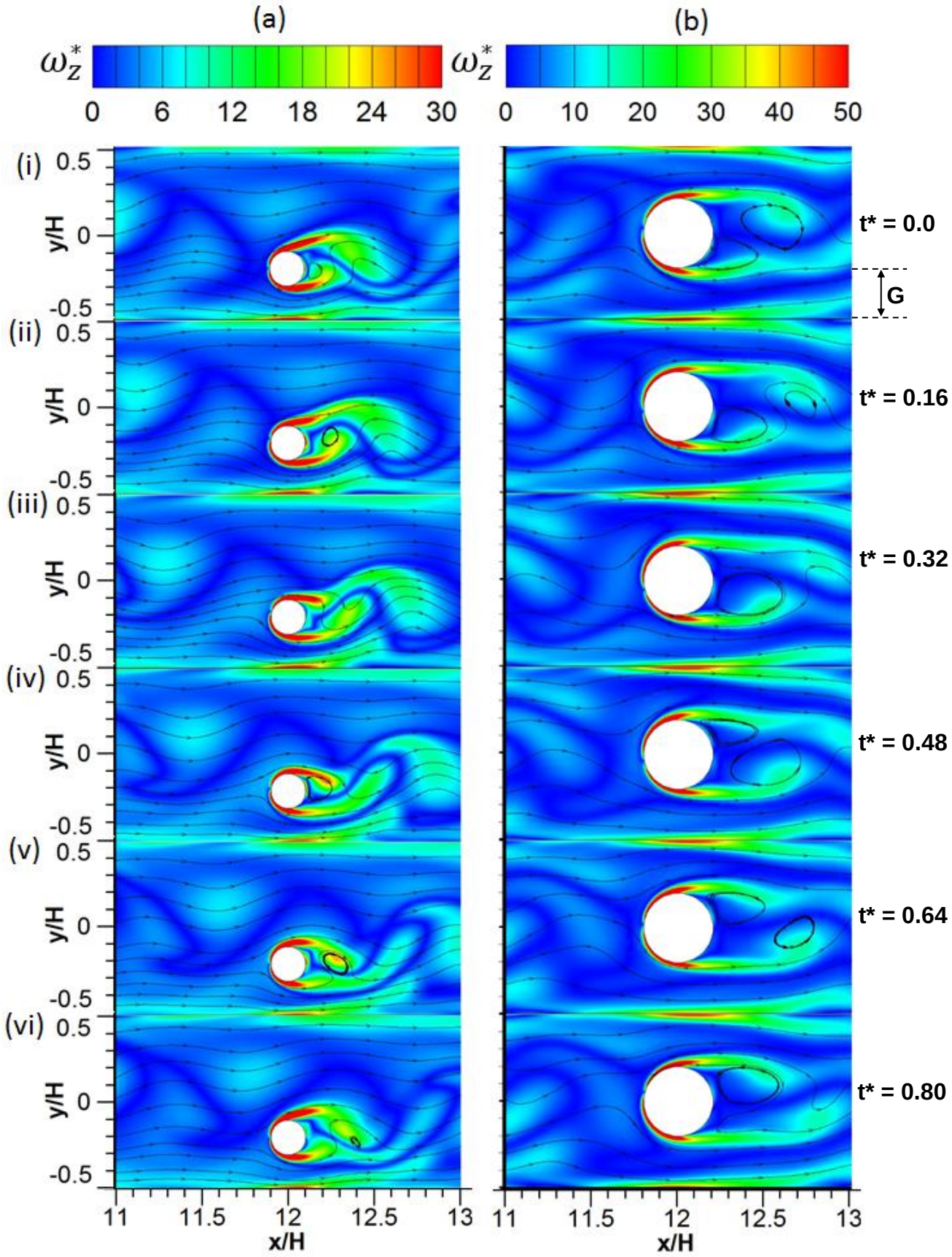

Figure 11. Instantaneous normalized z-vorticity, ω_z^* and streamlines with time stamp, t* at Re = 920, θ = 90° (computations): (a) d/p = 0.05, d = 5 mm, staggered; (b) d/p = 0.2, d = 10 mm, in-line. Normalized time steps Δt* = 0.16, $\omega_z^* = \frac{\omega_z H}{V_{avg}}$, $t^* = \frac{t\, V_{avg}}{H}$.

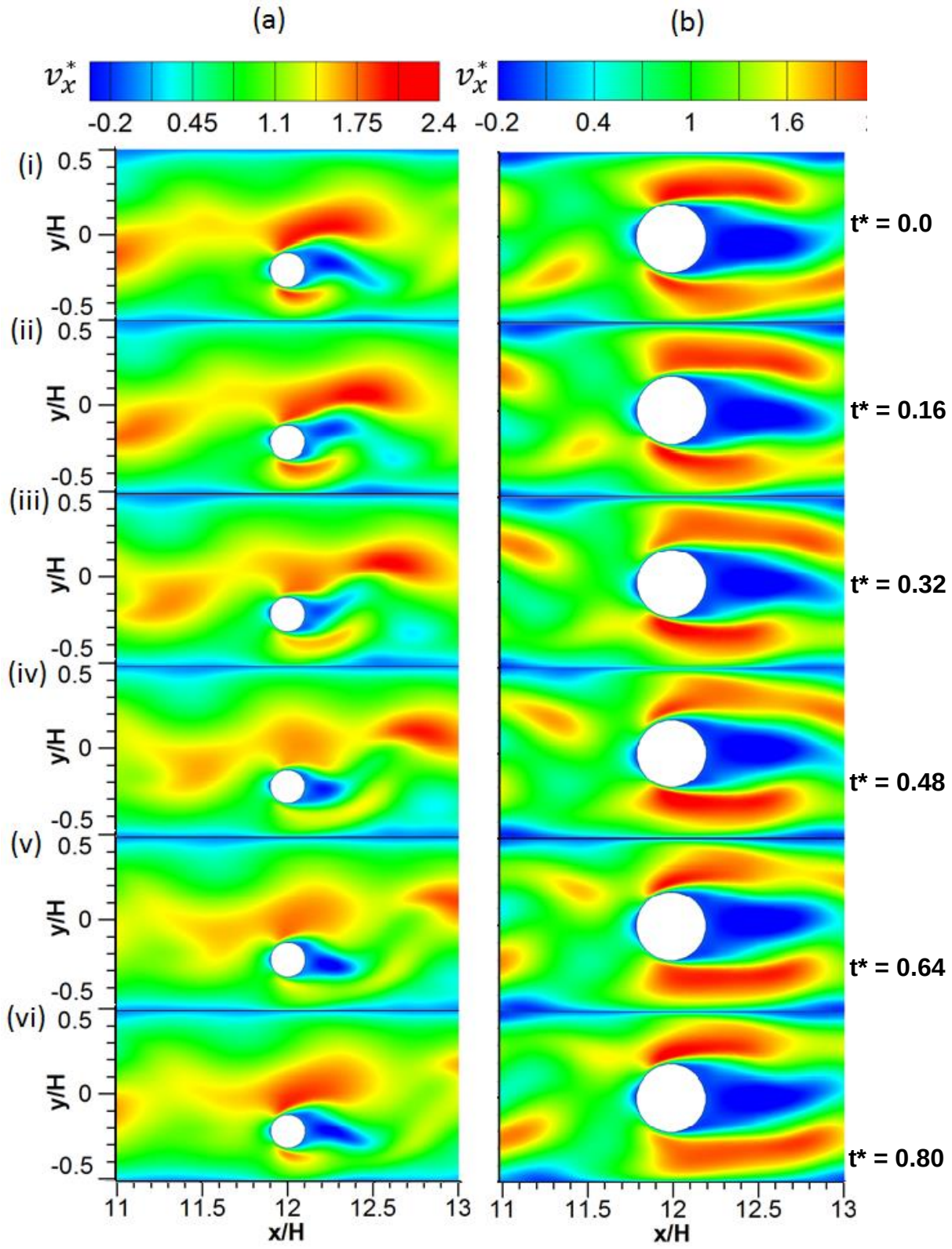

Figure 12. Instantaneous normalized x-velocity, v_x^* with time stamp, t* at Re = 920, θ = 90° (computations): (a) d/p = 0.05. d = 5 mm, staggered; (b) d/p = 0.2, d = 10 mm, in-line. Normalized time steps Δt* = 0.16.

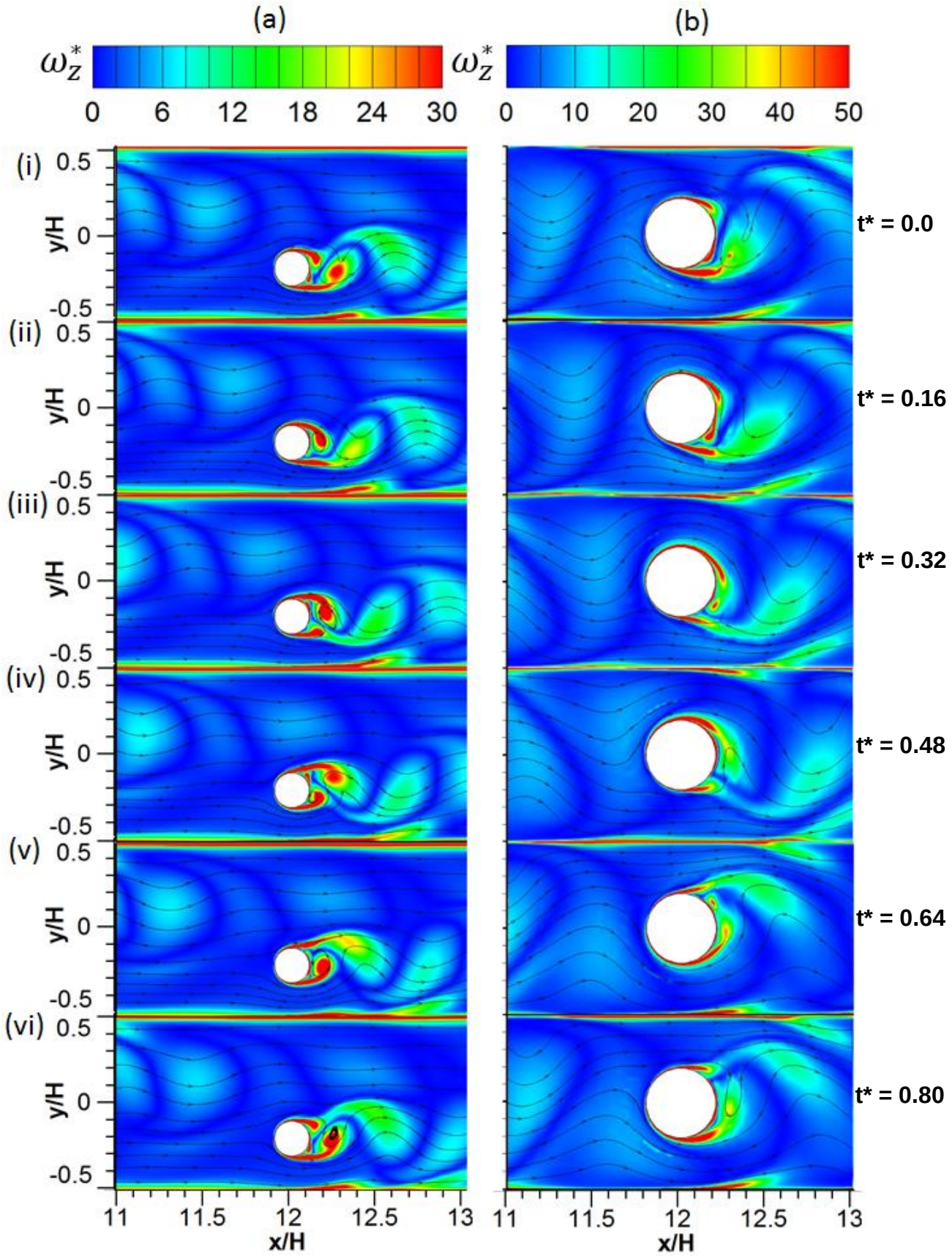

Figure 13. Instantaneous normalized z-vorticity, ω_z^* and streamlines with time stamp, t* at Re = 9700, θ = 90° (computations): (a) d/p = 0.05. d = 5 mm, staggered; (b) d/p = 0.2, d = 10 mm, in-line. Normalized time steps Δt* = 0.16.

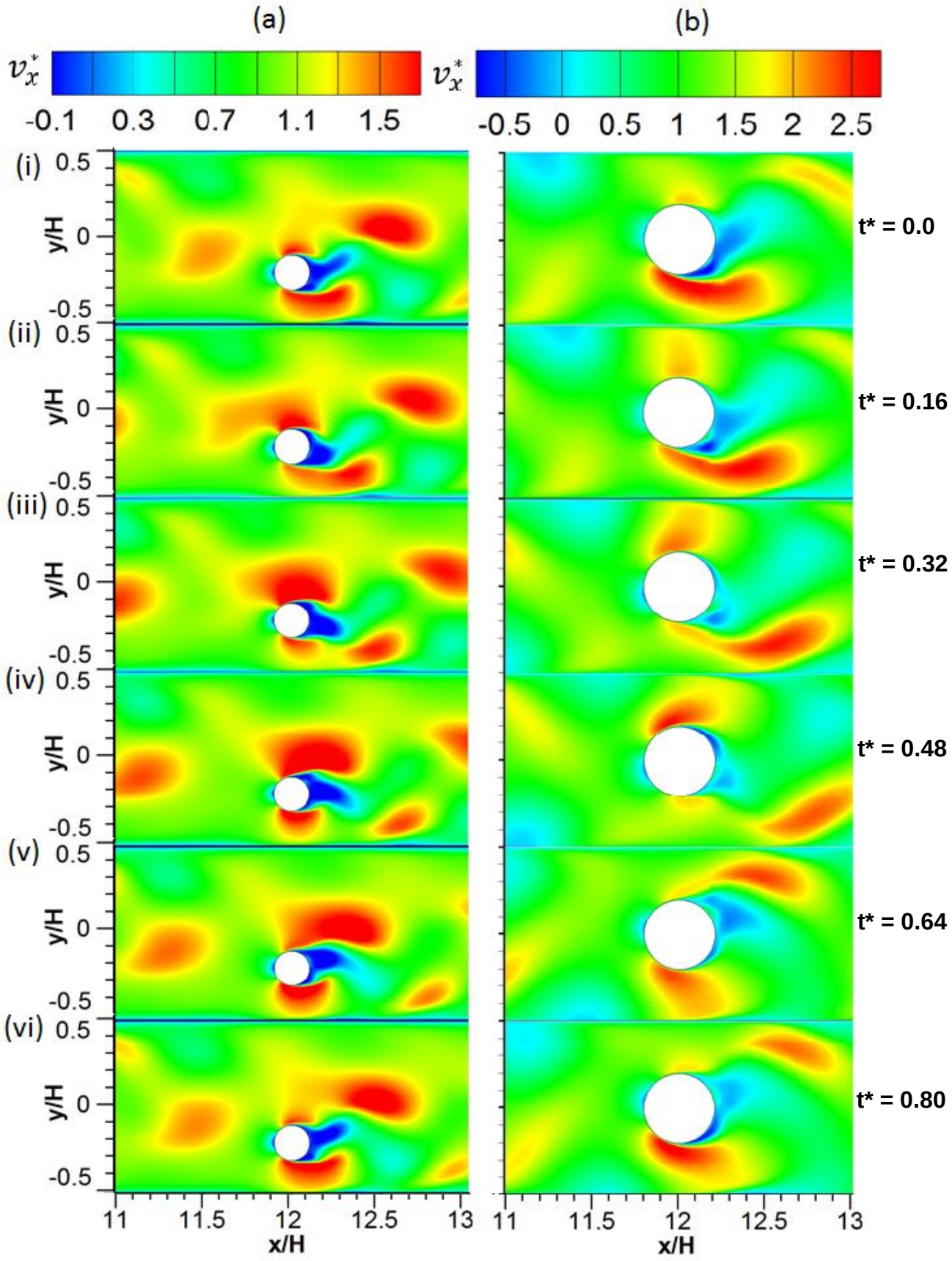

Figure 14. Instantaneous normalized x-velocity, v_x^* with time stamp, t* at Re = 9700, θ = 90° (computations): (a) d/p = 0.05. d = 5 mm, staggered; (b) d/p = 0.2, d = 10 mm, in-line. Normalized time steps Δt* = 0.16.

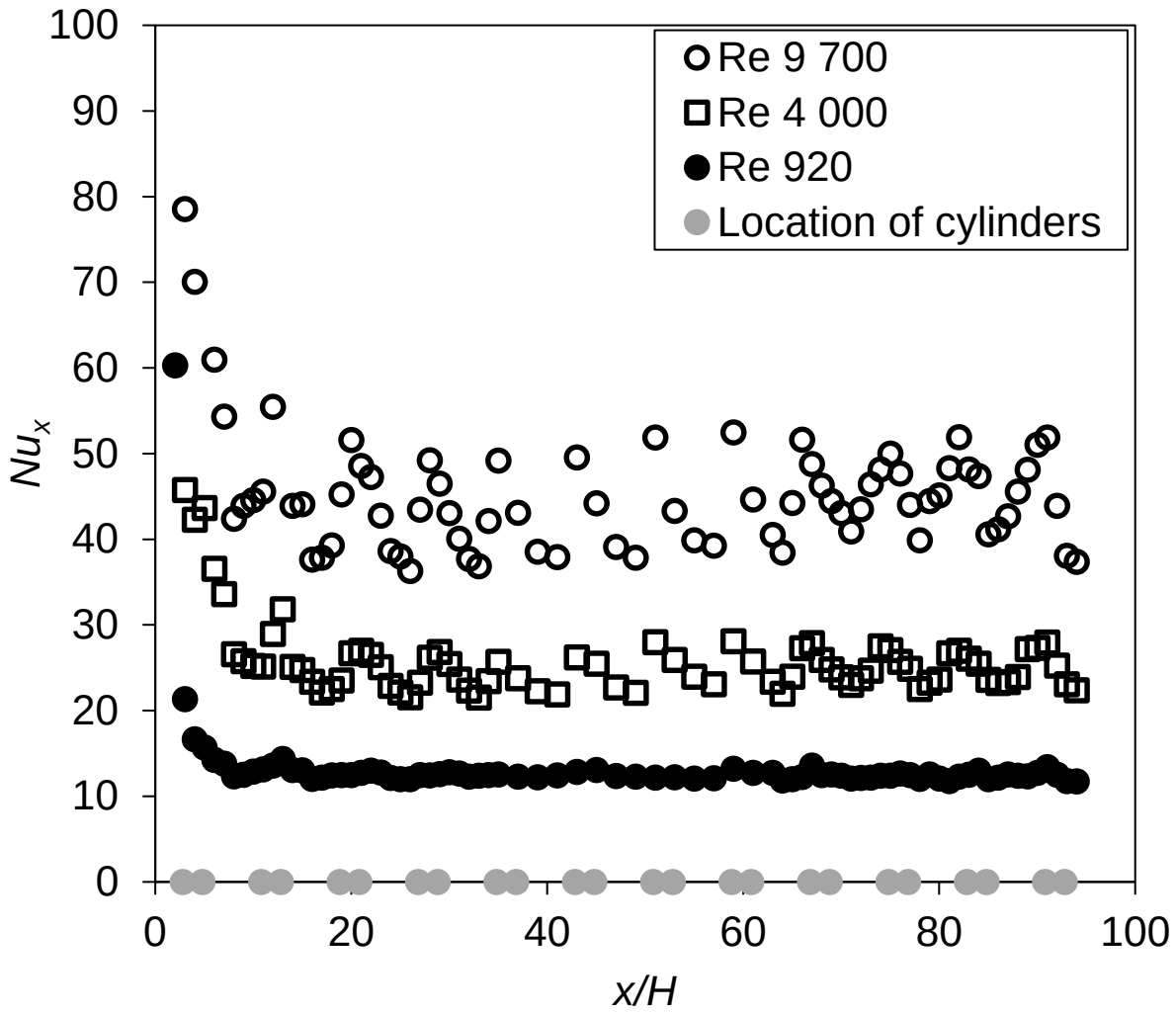

Figure 15. Time-averaged local Nusselt number (Nu_x) distributions along channel wall (x/H) at Re = (920 – 9700) for staggered cylinder array: d/p = 0.025, θ = 90°, d = 1 mm, H = 5 mm.

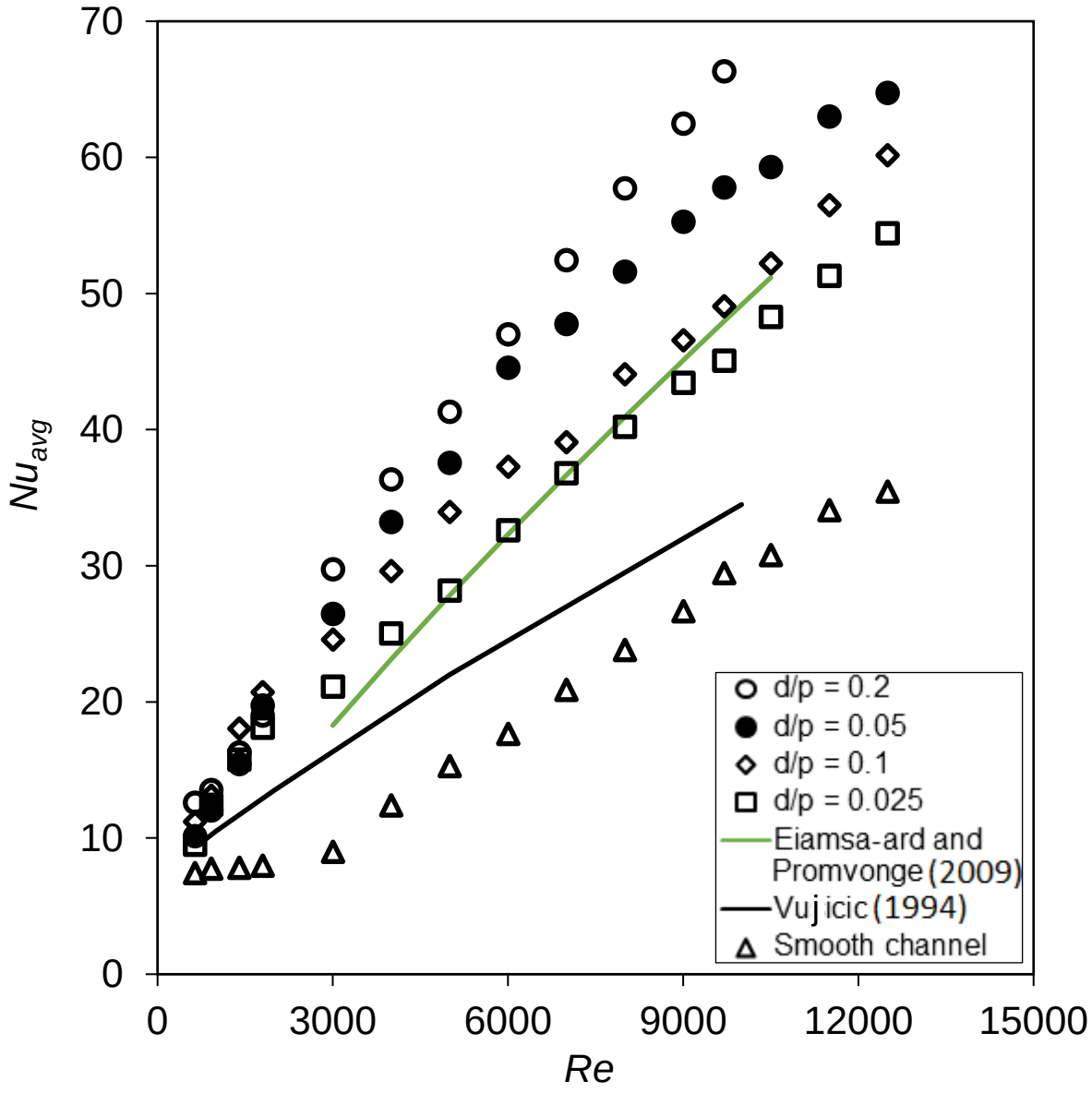

Figure 16. Average Nusselt number (Nu_{avg}) plotted against Re for cylinder arrays with θ = 90°: (d/p = (0.1, 0.2), d = 2 mm, in-line) and (d/p = (0.025, 0.05), d = 1 mm, staggered). Smooth channel: no cylinders.

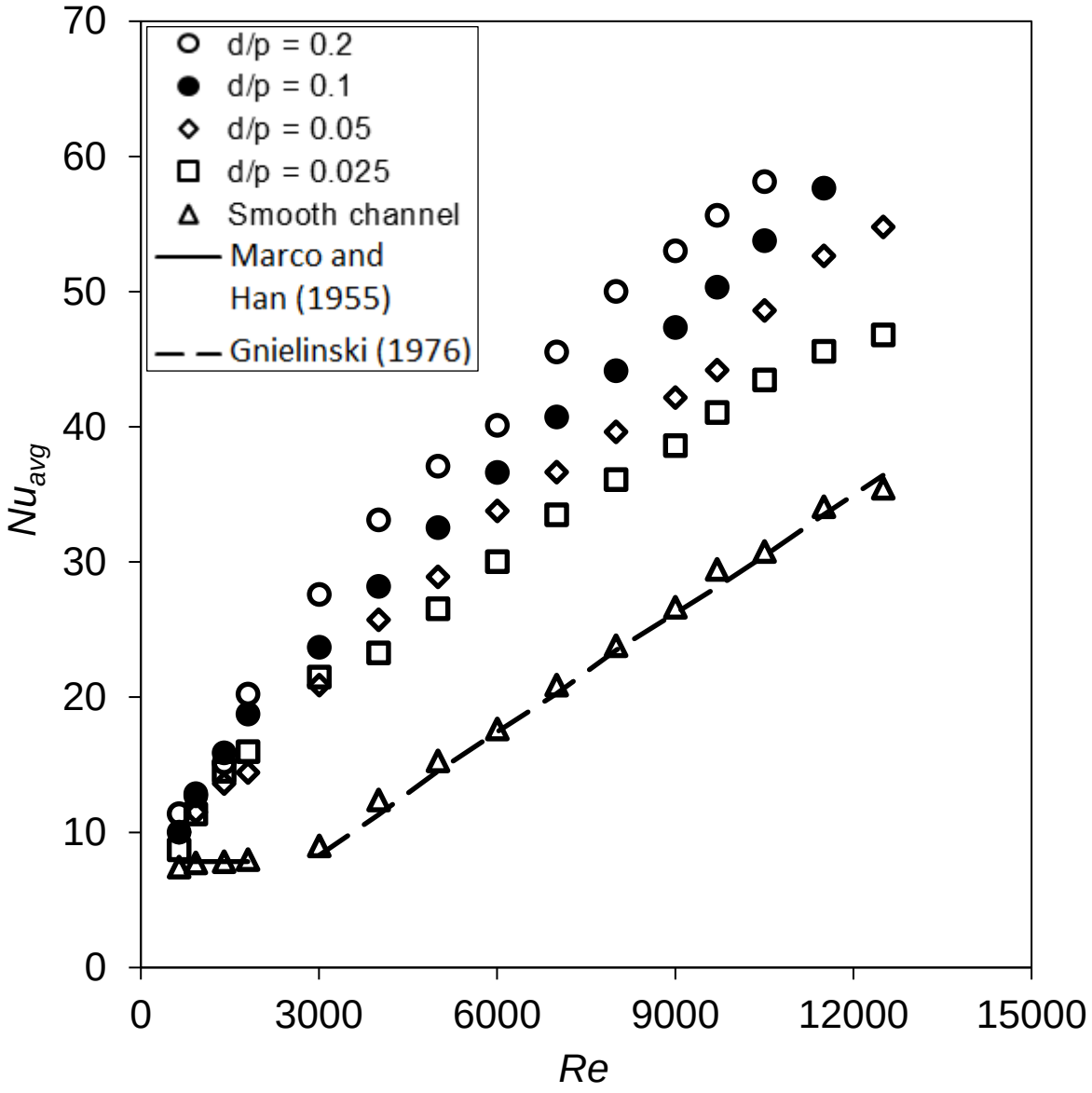

Figure 17. Average Nusselt number (Nu_{avg}) plotted against Re for cylinder arrays with θ = 45°: (d/p = (0.1, 0.2), d = 2 mm, in-line) and (d/p = (0.025, 0.05), d = 1 mm, staggered).

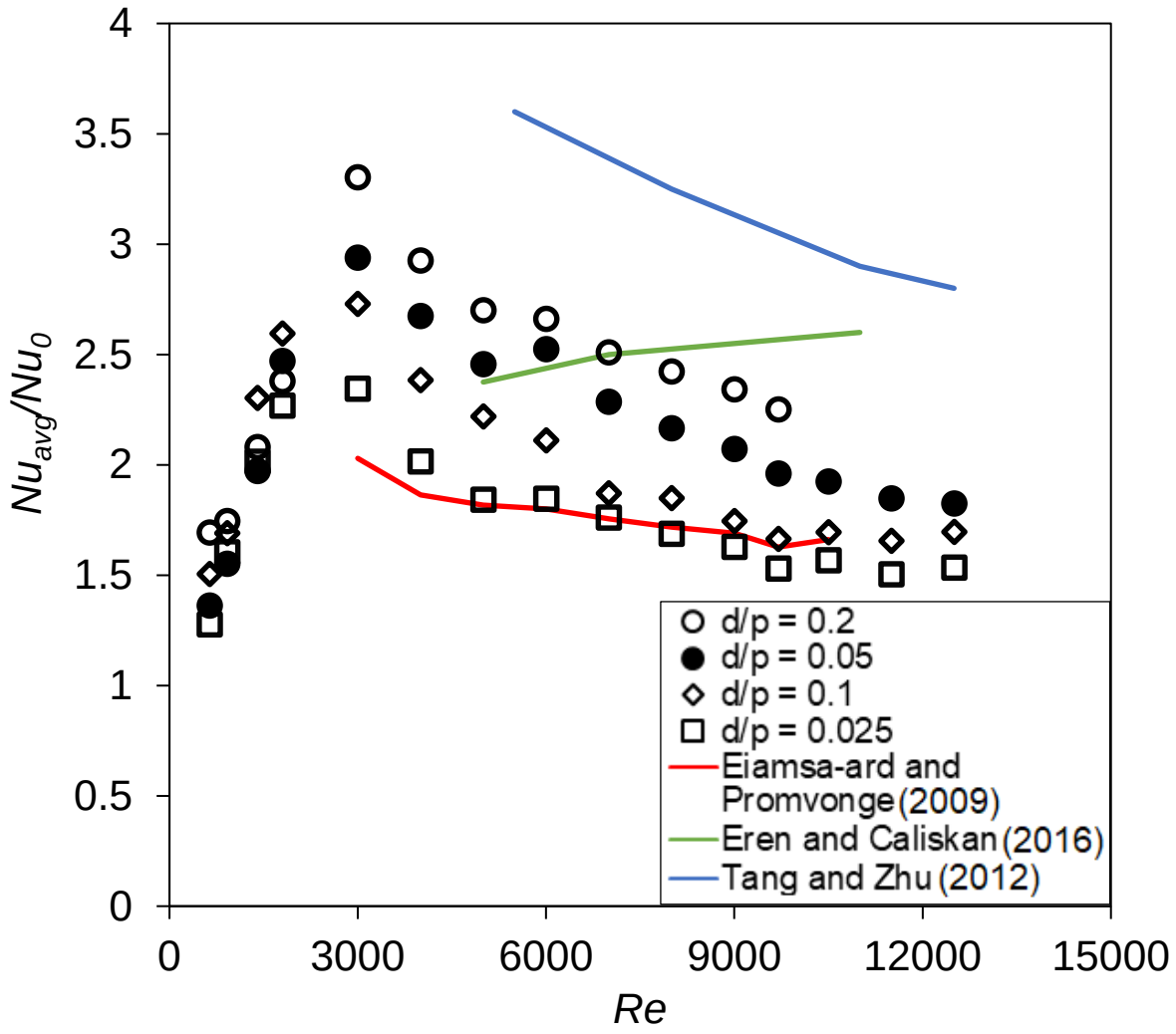

Figure 18. Nusselt number ratio of cylinder array to smooth channel (Nu_{avg}/Nu_0) plotted against Re for cylinder arrays with θ = 90°: (d/p = (0.1, 0.2), d = 2 mm, in-line) and (d/p = (0.025, 0.05), d = 1 mm, staggered).

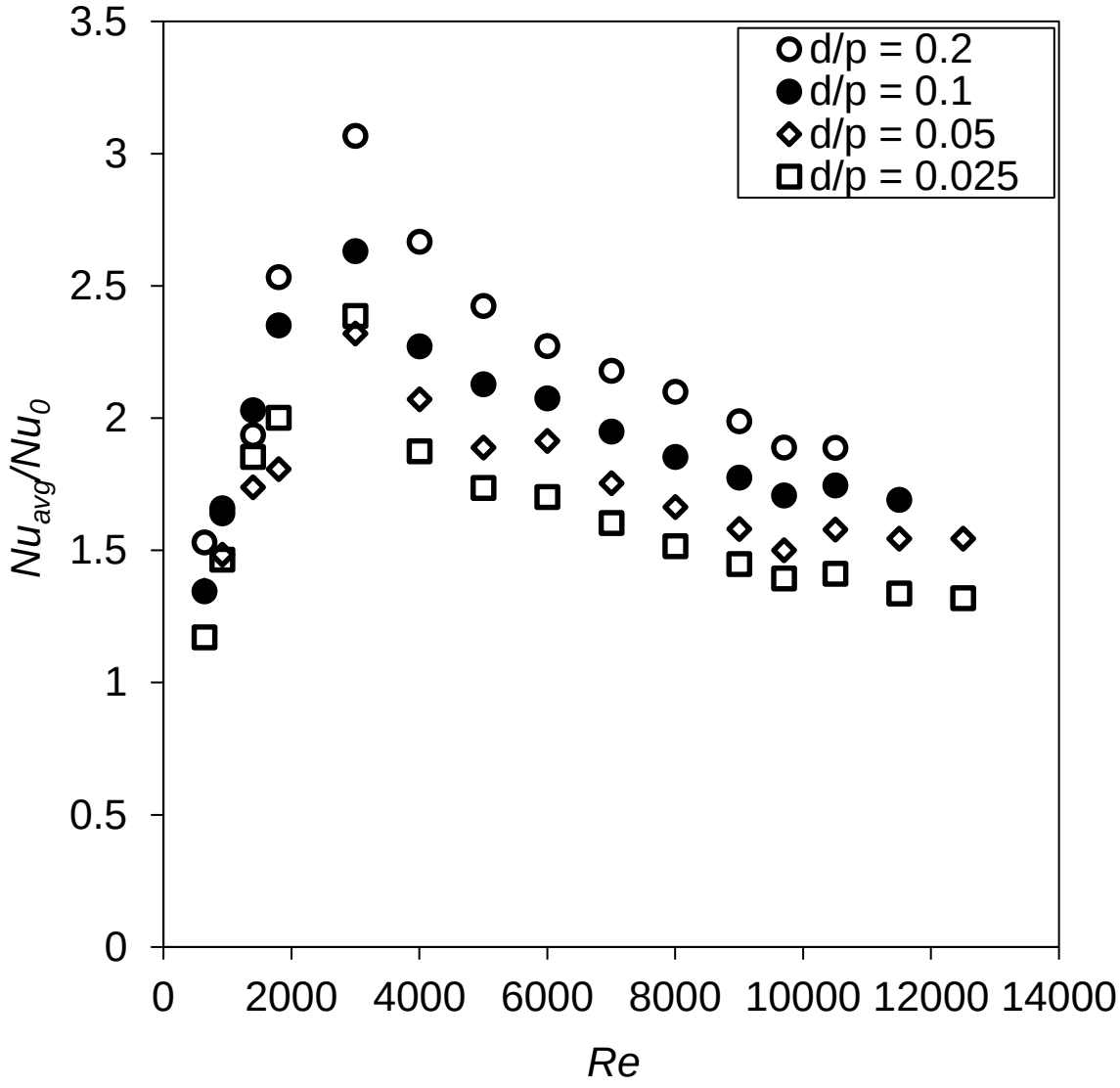

Figure 19. Nusselt number ratio of cylinder array to smooth channel (Nu_{avg}/Nu_0) plotted against Re for cylinder arrays with θ = 45°: (d/p = (0.1, 0.2), d = 2 mm, in-line) and (d/p = (0.025, 0.05), d = 1 mm, staggered).

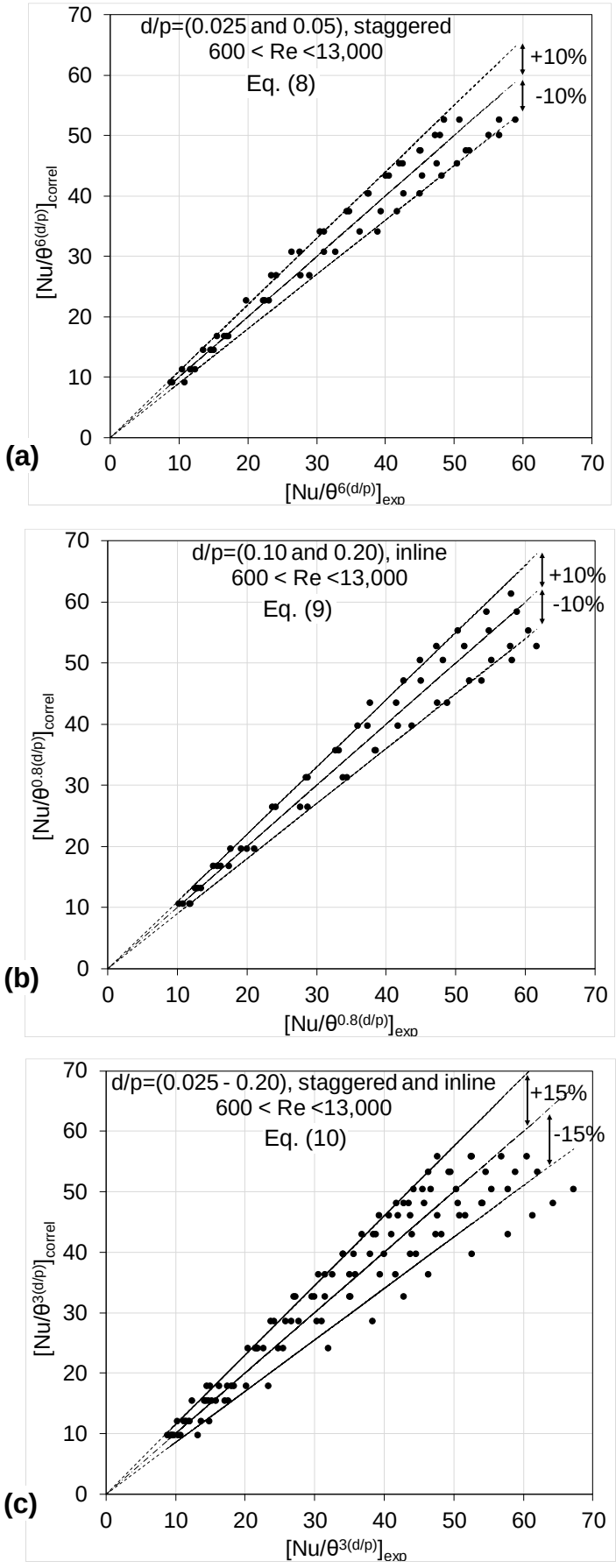

Figure 20. Comparisons between calculated $[Nu/\theta^{n)}]_{correl}$ from Eqs. (8-10) and experimental $[Nu/\theta^{n}]_{exp}$ for: (a) n = 6(d/p), staggered; (b) n = 0.8(d/p), in-line; (c) n= 3(d/p), staggered and in-line.

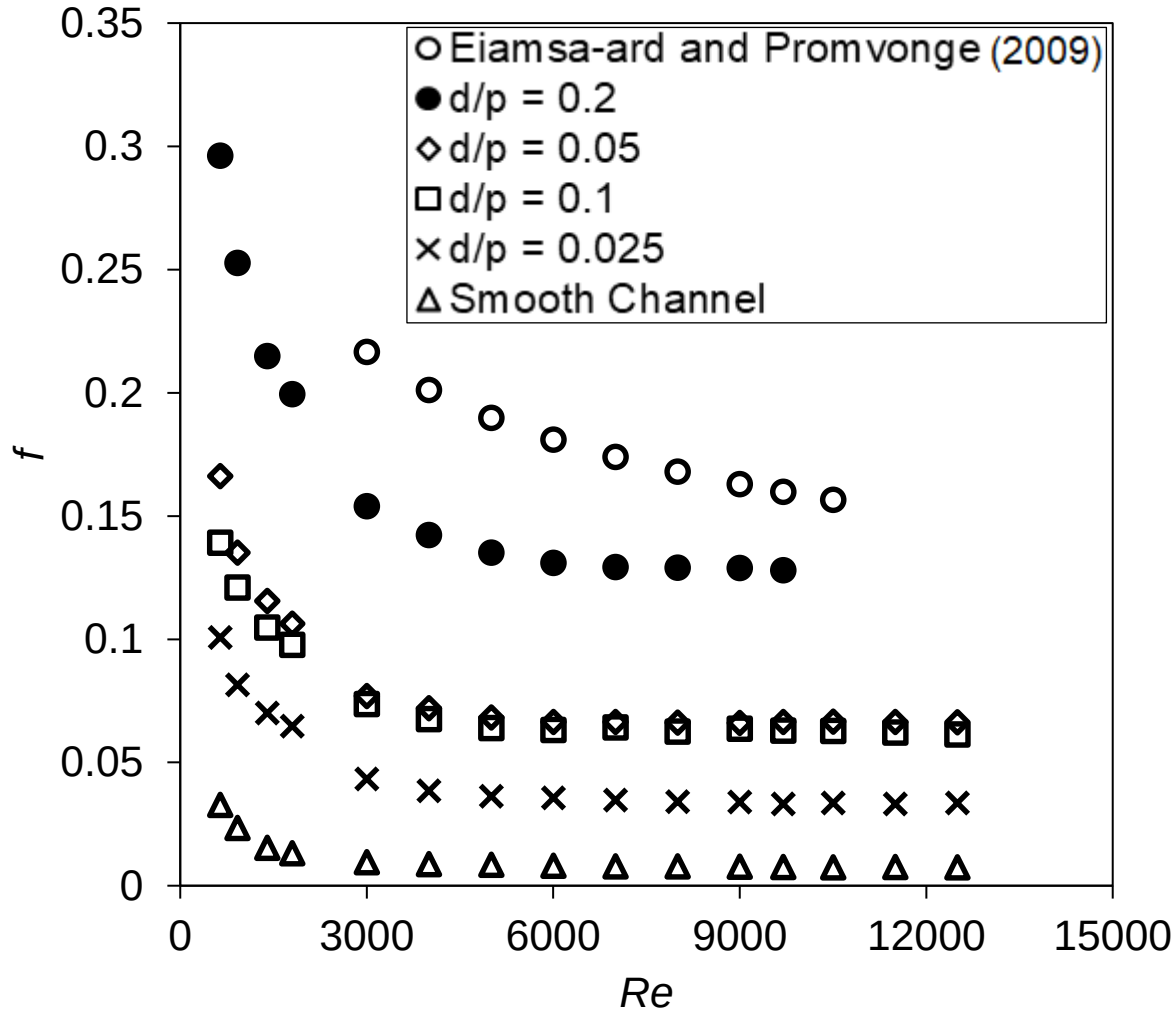

Figure 21. Friction factor (f) plotted against Re for cylinder arrays with θ = 90°: (d/p = (0.1, 0.2), d = 2 mm, in-line) and (d/p = (0.025, 0.05), d = 1 mm, staggered).

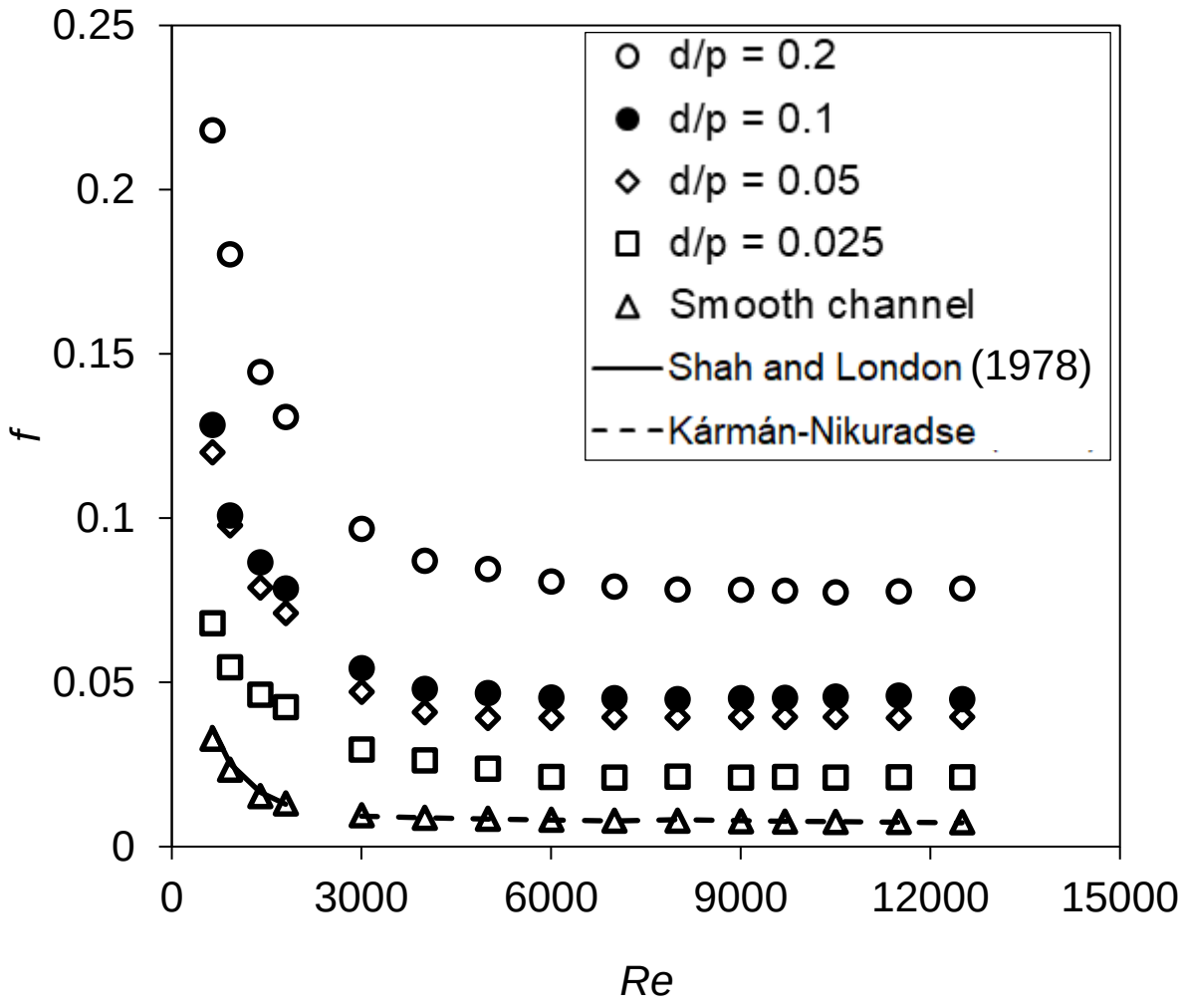

Figure 22. Friction factor (f) plotted against Re for cylinder arrays with θ = 45°: (d/p = (0.1, 0.2), d = 2 mm, in-line) and (d/p = (0.025, 0.05), d = 1 mm, staggered).

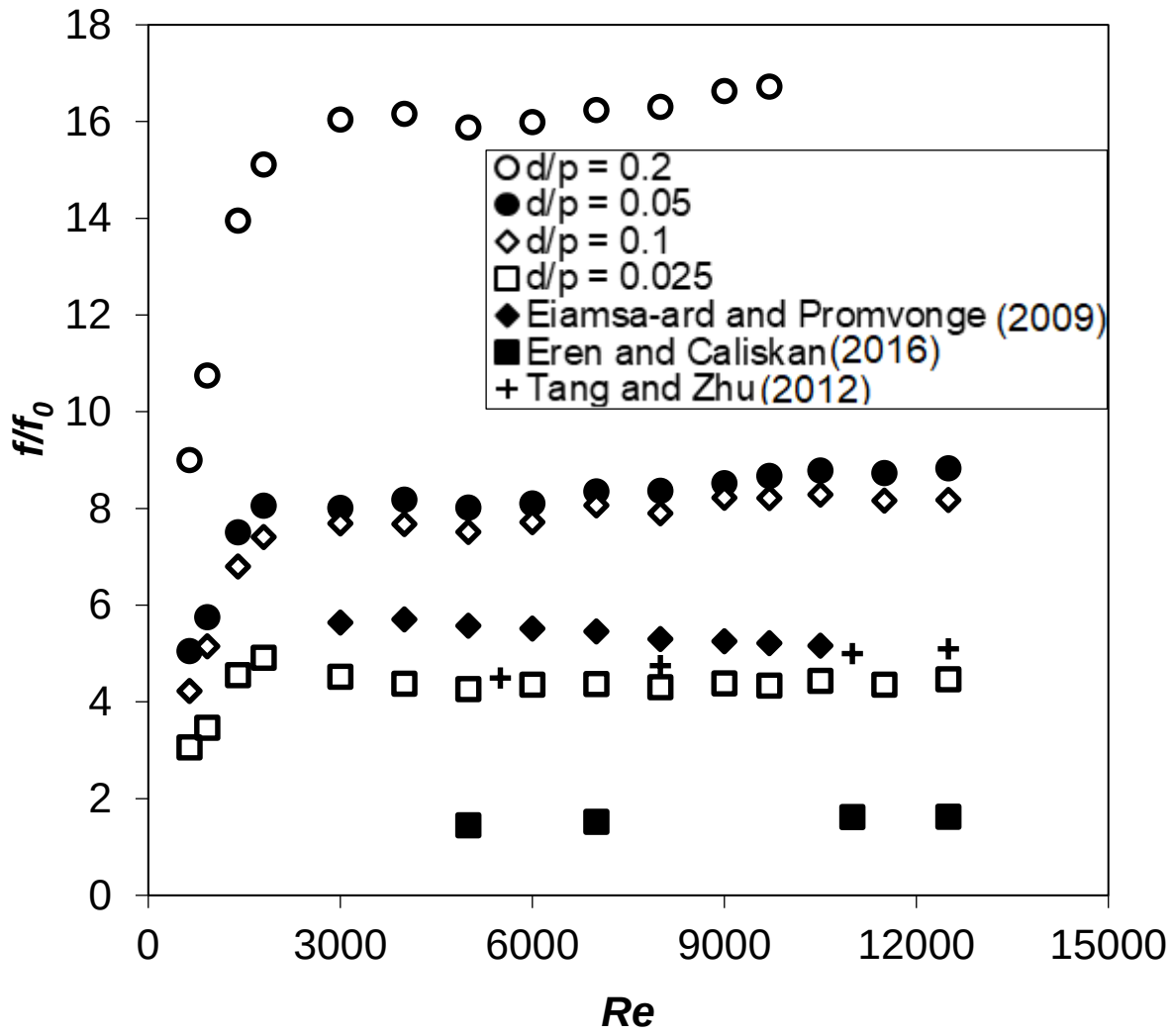

Figure 23. Friction factor ratio (f/f_0) plotted against Re for cylinder arrays with $\theta = 90°$: (d/p = (0.1, 0.2), d = 2 mm, in-line) and (d/p = (0.025, 0.05), d = 1 mm, staggered).

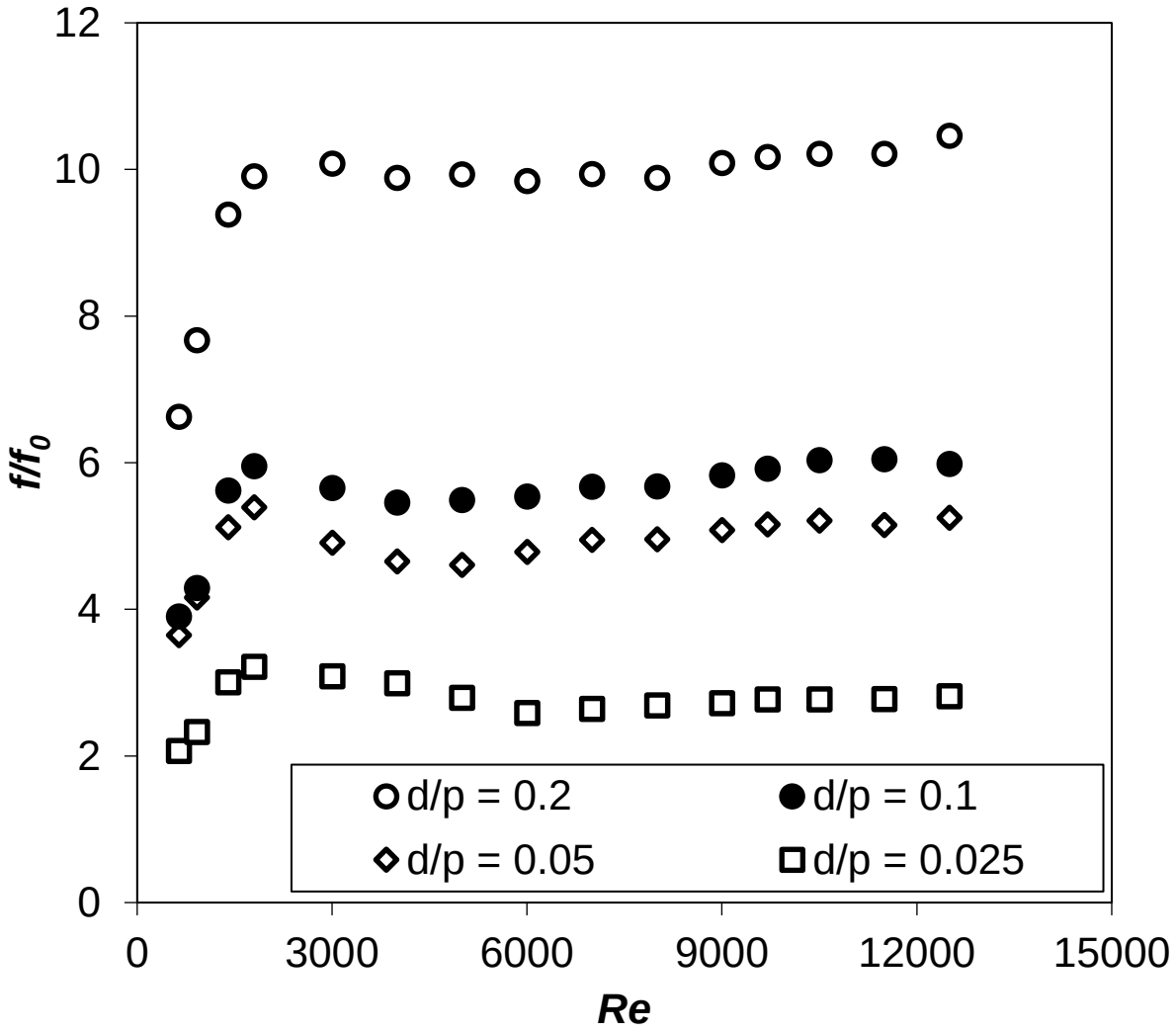

Figure 24. Friction factor ratio (f/f_0) plotted against Re for cylinder arrays with $\theta = 45°$: (d/p = (0.1, 0.2), d = 2 mm, in-line) and (d/p = (0.025, 0.0.05), d = 1 mm, staggered).

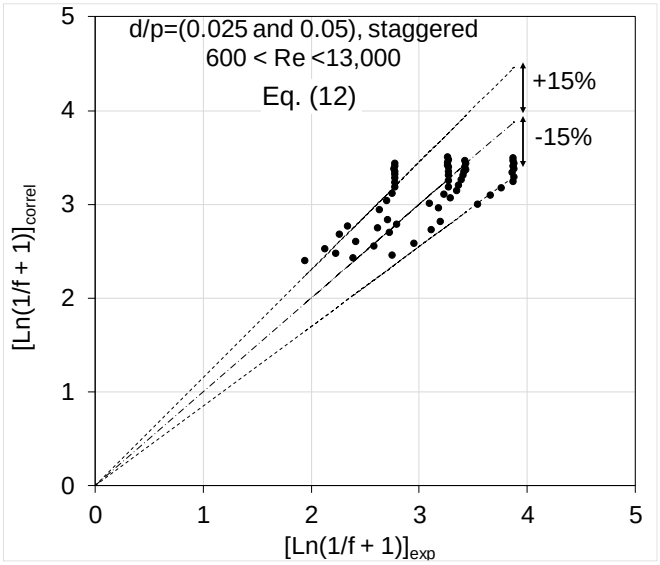

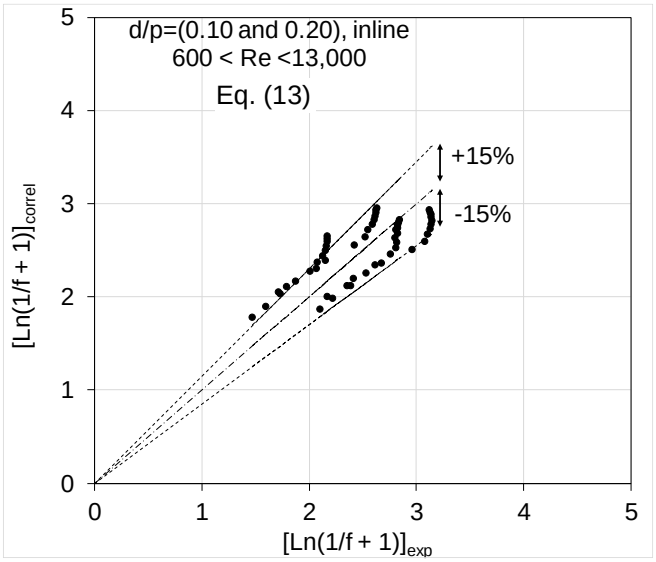

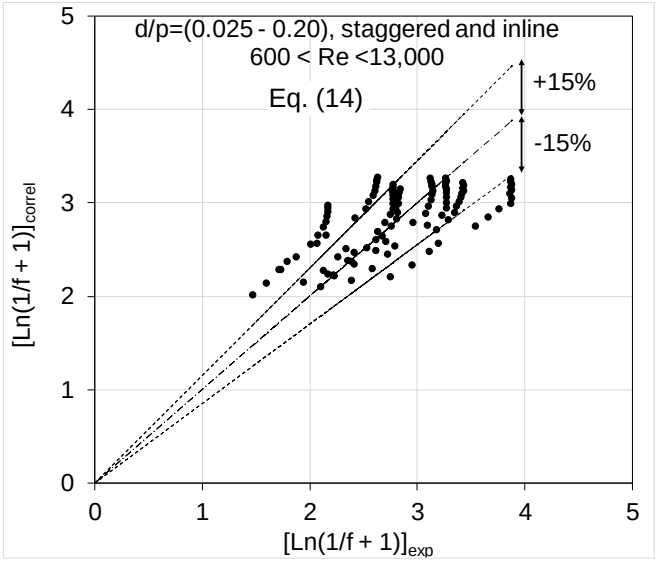

Figure 25. Comparisons between calculated $[Ln(1/f+1)]_{correl}$ from Eqs. (12-14) and experimental $[Ln(1/f+1)]_{exp}$ for: (a) staggered arrays; (b) in-line arrays; (c) staggered and in-line arrays.

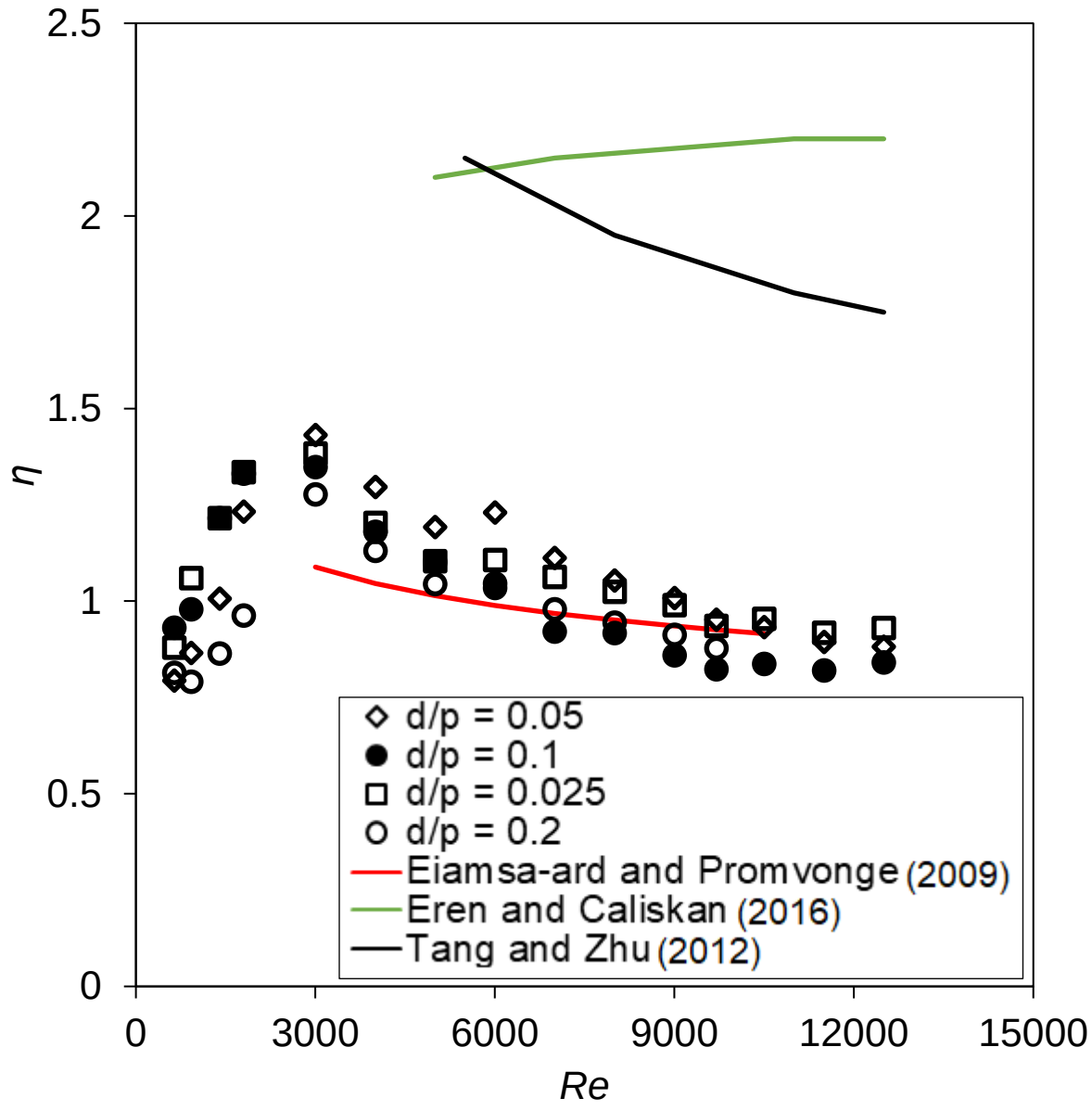

Figure 26. Thermal performance coefficient (η) plotted against Re for cylinder arrays with θ = 90°: (d/p = (0.1, 0.2), d = 2 mm, in-line) and (d/p = (0.025, 0.0.05), d = 1 mm, staggered).

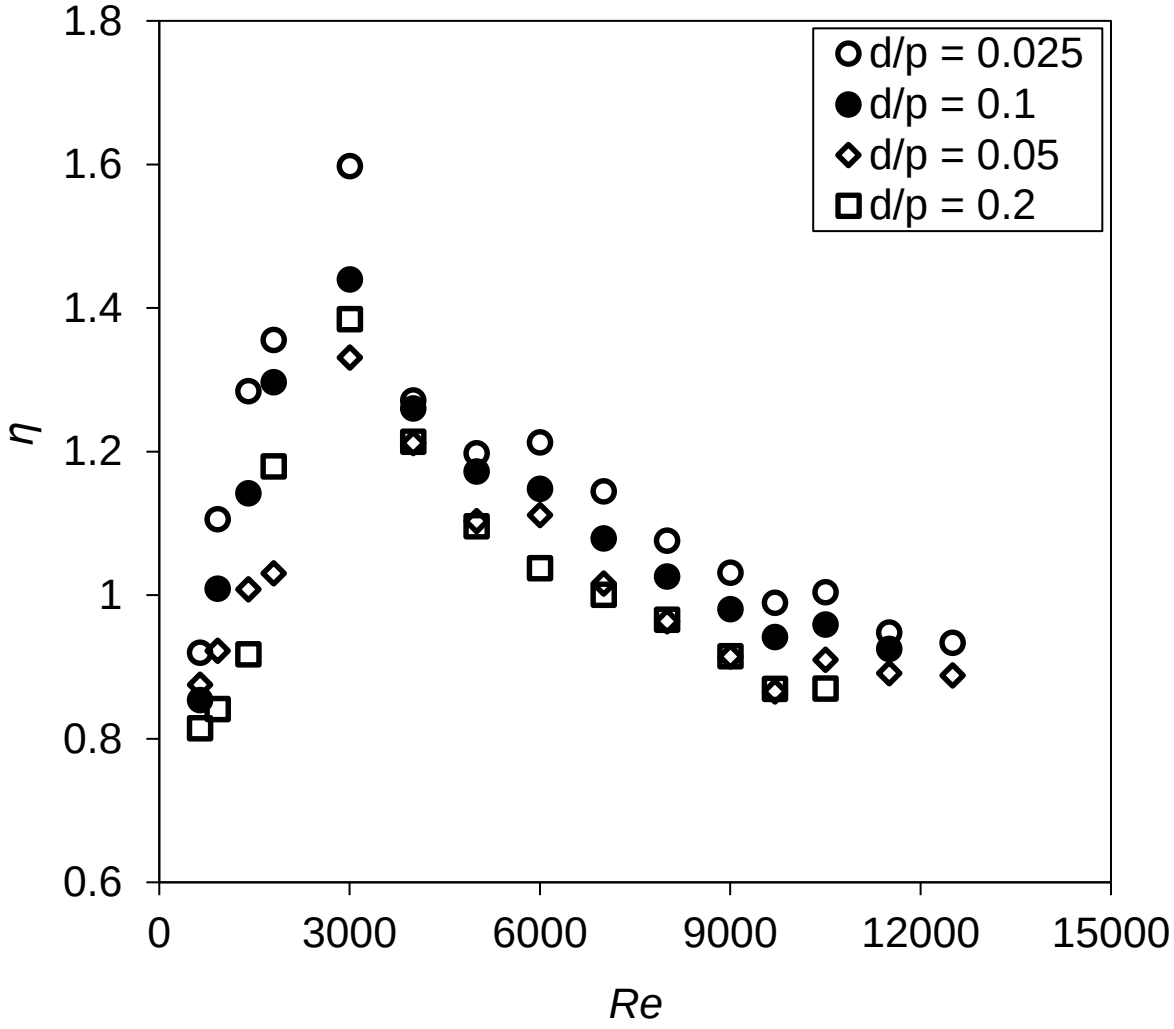

Figure 27. Thermal performance coefficient (η) plotted against Re for cylinder arrays with θ = 45°: (d/p = (0.1, 0.2), d = 2 mm, in-line) and (d/p = (0.025, 0.0.05), d = 1 mm, staggered).